

MSc Chemistry
Molecular Sciences

MASTER THESIS

**Nucleation Study of the Electrochemical
Deposition of Silver on Indium Tin Oxide**

by

Mees Dieperink

Student number UvA: 11239190

Student number VU: 2605636

48 ECTS

November 2020 – July 2021

1st Examiner:

prof. dr. Fred Brouwer

2nd Examiner:

dr. Andrea Baldi

Main supervisor:

dr. Esther Alarcón Lladó

Daily supervisor:

Yorick Bleiji

AMOLF Amsterdam, The Netherlands, July 17, 2021



Nucleation Study of the Electrochemical Deposition of Silver on Indium Tin Oxide

Mees Dieperink

3D Photovoltaics, AMOLF
1098 XG Amsterdam, The Netherlands

July 17, 2021

Abstract

The electrodeposition of Ag nanoparticles on ITO has a high nucleation barrier and previous research has shown that it is a challenge to electrochemically control the particle density and particle size. This originates from complex nucleation kinetics that arise from the low surface energy of ITO and electrolyte-specific electrochemical parameters. This thesis attempts to elucidate such nucleation mechanisms by performing chronoamperometry experiments using the double-pulse technique. The effect of the nucleation overpotential for ITO batches with different crystal orientations has been investigated. Particle analyses from SEM and AFM were successfully linked to fits from growth models, such that different nucleation mechanisms were identified per ITO batch. This underlines the importance of substrate characterization for electrodeposition and opens up the possibility of utilizing the surface properties. Moreover, it was concluded that the nucleation potential effectively controls the particle density and particle size during nucleation.

1	Introduction	1
2	Theory	3
2.1	Introduction to electrochemistry	3
2.2	Electrochemical setup	5
2.2.1	Working electrode	5
2.2.2	Counter electrode	5
2.2.3	Reference electrode	5
2.3	Electrochemical techniques	5
2.3.1	Cyclic voltammetry	6
2.3.2	Chronoamperometry	8
2.4	Electrocrystallization	8
2.5	Electrochemical deposition of Ag on ITO	9
2.5.1	Double-pulse technique	10
2.5.2	Growth models	11
3	Fabrication	15
3.1	Sample preparation	15
3.2	Electrolyte preparation	16
3.3	Electrochemical cell	16
3.4	Typical experiment	17
4	Characterization	19
4.1	Scanning Electron Microscopy	19
4.2	Energy-Dispersive X-ray spectroscopy	20
4.3	X-ray Diffraction spectroscopy	21
4.4	Atomic Force Microscopy	21
5	Results and Discussion	23
5.1	ITO characterization	23
5.2	The choice of electrolyte	23

5.3	Particle analysis	25
5.4	The effect of E_n – saccharin-based electrolyte	27
5.5	Chronoamperometry analysis	30
5.6	Growth analysis	33
6	Conclusion and Outlook	35
	References	40
	Acknowledgements	41
	Appendix	43
A1	Reference electrode performance	43
A2	Miscellaneous	43
A3	Potentiostat performance	46
A4	EC-lab	47
A5	XRD peak height ratios	48
A6	Cyclic voltammetry models	48
A7	ImageJ analysis	50
A8	Self-assembled monolayers	51

Electroplating is a prominent technique for surface treatment that is used to introduce new functionalities in substrates. Various industries finish their products with an electroplated coating, such as automotive, aerospace and medical manufacturing [1]. Currently, 18000 treatment installations are operational in Europe and the global electroplating market in 2020 is estimated at \$15 billion [1–3]. On one hand, the demand for electroplating arises from the production of aesthetically pleasing products. On the other hand, materials used to produce industrial machinery need coatings as they are prone to corrosion and tribological degradation. Coating these materials by means of electroplating can increase their functional lifetime significantly.

Electroplating originates from the late 18th century and early examples of reported experiments are gold plating of a silver coin by Brugnatelli in 1801 and isolation of sodium from molten salts by Davy in 1807 [4]. Shortly afterwards, Faraday developed the theoretical basis for electrochemistry and, combined with Maxwell’s electromagnetic theory, experiments with reliable electricity sources could be conducted. In 1840, Wright introduced cyanide-based solutions into the field and he succeeded in manufacturing a Ni-Ag alloy (German silver). Cyanide-based solutions are still used extensively nowadays because of their excellent electrochemical properties, especially in the electroplating of Ag. However, cyanide is highly toxic for living organisms and from a sustainable perspective its use in electroplating should be prevented [5, 6].

Nevertheless, Ag electrodeposition with cyanide finds numerous industrial applications because of the high bulk conductivity, good corrosion resistance and antibacterial properties of Ag, and the simplicity and low cost of electroplating opposed to vapour deposition techniques [7]. Therefore, research is performed on cyanide-free alternatives for Ag electroplating that involve, ionic liquids, thiosulfate baths, [8] combinations of organic additives, [9, 10], and even plant extracts [11]. State-of-the-art substrates for Ag electrodeposition are Cu, Au or other similar metals that complicate spectroscopic analyses. Hence, it is interesting to study the deposition of Ag on more transparent materials. Surface enhanced Raman spectroscopy (SERS) is an example of such a technique and a well-studied system consists of Ag nanoparticles (electro)deposited on indium tin oxide (ITO) [12–14]. Next to facilitating spectroscopic analyses, ITO is heavily used in optoelectronic devices and effective metallization could improve its integration [15].

To our knowledge, only a few groups (Sandmann et al., Hau et al. and Ueda et al.) have studied the direct electroplating of Ag on ITO and only Hau et al. used a cyanide-free

solution. These articles show that it is a challenge to electrodeposit a continuous film of Ag on ITO because of its relatively high sheet resistance and low surface energy. Moreover, the different crystal orientation of Ag and ITO causes stress and strain during deposition, resulting in poor adhesion. To overcome this high nucleation barrier and effectively grow particles [Sandmann et al.](#), [Hau et al.](#) and [Ueda et al.](#) employed the double-pulse technique, which will be explained in Chapter 2.

This thesis focuses on a nucleation study that involves the electrochemical deposition of Ag on ITO using the double-pulse technique. The goal was to identify electrochemical parameters with which the density and size of Ag nanoparticles can be controlled. To gain a better understanding of nucleation mechanisms, two ITO batches were used that had a different preferred crystal orientation according to XRD measurements. Particle analyses from SEM and AFM were combined with chronoamperometry modeling to explain both the nucleation mechanism and growth direction in electrodeposition experiments.

The outline of this thesis is:

- Chapter 2 presents an introduction to electrochemistry, an explanation of several electrochemical techniques, and overviews of electrocrystallization, the double-pulse technique and developed growth models.
- Chapter 3 discusses the experimental details and elaborates on sample and electrolyte preparation, handling of the electrochemical cell and execution of a typical electrodeposition.
- Chapter 4 explains the used characterization techniques, including SEM, EDX, XRD and AFM.
- Chapter 5 analyzes the obtained results from electrodepositions with the saccharin-based electrolyte on two different batches of ITO.

This chapter provides an introduction to electrochemistry and elaborates on several electrochemical techniques. Subsequently, the general theory of electrocrystallization is discussed, after which the introduced concepts are linked to the double-pulse technique. Finally, an overview is given of the developed growth models for single-pulse chronoamperometry experiments.

2.1 Introduction to electrochemistry

Electrochemistry involves the exchange of electrical and chemical energy such that either charge is transferred by a chemical reaction, or that chemistry is driven by an electrical current [16, 17]. This interplay of ions and electrons becomes possible with a conductive solid and liquid, called an electrode and electrolyte, respectively. The electrochemical reaction will take place at the solid-liquid interface and the direction of charge transport defines whether a reduction (2.1) or oxidation (2.2) reaction is taking place. Upon combining both half reactions one can perform a complementary redox reaction, for which two electrodes are necessary. At the cathode a reduction will occur, while at the anode an oxidation takes place.



The spontaneity of reactions is determined by the standard Gibbs free energy ΔG° , which is defined by the available charge and standard electrical potential (2.3) [16, 17]. When ΔG° is negative the reaction occurs spontaneously and electrical energy is generated. When ΔG° is positive the reaction is non-spontaneous and external electrical energy is necessary to drive the reaction.

$$\Delta G^\circ = -qE^\circ \quad \text{with} \quad q = nF \quad (2.3)$$

where E° is the standard potential, q the charge, n the amount of involved electrons and F Faraday's constant. However, this equation only holds for standard conditions, which means that all reactant activities are equal to 1. Once a system deviates from this, reactants

will show non-standard reaction activities resulting in a different Gibbs free energy. To find the altered electrical potential for this system one can use the Nernst equation (2.4) which corrects for non-standard reactant activities. Note that the sign of the potential depends on the choice of half reaction and that temperature plays a role in the potential shift as well.

$$E = E^\circ - \frac{RT}{nF} \ln \frac{a_{red}}{a_{ox}} \quad (2.4)$$

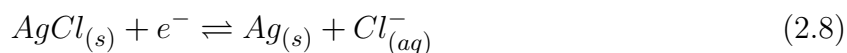
where R is the universal gas constant, T the temperature and a_{red} and a_{ox} the activities of the reductant and oxidant, respectively. Equation 2.4 can be rewritten in terms of formal potential $E^{\circ'}$ by converting the activities to concentrations with activity coefficients ($a = \gamma c$):

$$E = E^{\circ'} - \frac{RT}{nF} \ln \frac{c_{red}}{c_{ox}} \quad (2.5)$$

Since the potential scale is relative it is important to have a benchmark. A typical reference system is the standard hydrogen electrode (SHE) [18]. Hydrogen gas is bubbled through this electrochemical half cell with a pressure of 1 bar (100 kPa), while a platinum electrode is immersed in a theoretical solution of 1 M acid. The solution is theoretical in the sense that ions do not interact with each other, which means that the activity coefficient of protons will be unity. Under these conditions equation 2.6 will be in equilibrium, resulting in a relative potential of 0 V at any temperature.



Now, it is possible to measure the potential difference between SHE and another reference electrode, and in this thesis all potentials are reported against the saturated Ag/AgCl electrode. The corresponding half reactions are



and the simplified redox reaction is



By keeping the concentrations of each reactant constant a stable equilibrium potential is obtained. Measuring the potential difference between SHE and the Ag/AgCl electrode in a saturated KCl solution results in a potential of +0.197 V vs. SHE [16].

2.2 Electrochemical setup

Such reference electrodes can be used to monitor the potential in electrochemical cells, which allows for correct comparison between results of electrochemical experiments. A standard three-electrode configuration consists of a working electrode (WE), counter electrode (CE) and a reference electrode (RE). Current will flow between WE and CE and the potential of these electrons is measured between WE and RE.

2.2.1 Working electrode

The electrochemical reaction of interest takes place at the WE and, except in galvanic cells (or batteries), the electrode material remains intact. For this reason often noble metals (such as gold or platinum), carbon (such as glassy or pyrolytic forms) and semiconductors (such as indium tin oxide) are used.

2.2.2 Counter electrode

The CE is usually made up of an inert material such as platinum, gold or graphite and serves as charge provider or extractor. It is important that the area of the CE is larger than that of the WE so that charge transport does not limit the kinetics of the electrochemical reaction.

2.2.3 Reference electrode

Since electrolytes have a large solution resistance it is essential to bring RE in close proximity of WE. In this way, the ohmic drop is minimized and a more reliable potential is observed. In addition, an ideal RE is non-polarizable, which means that its potential does not change when a (small) current flows through the RE. To ensure this, the cell is separated from the electrolyte by a semi-permeable membrane that only allows the transport of protons and electrons. However, often other ions leak in or out of the RE affecting its equilibrium potential. Appendix [A1](#) demonstrates that over time the equilibrium potential shifts and eventually saturates, which requires the RE to be replaced.

2.3 Electrochemical techniques

In this work, a non-spontaneous reaction is described that will run when current starts flowing after overcoming a potential barrier. To control this potential, a potentiostat is used that applies a voltage to the CE in order to reach the specified potential between WE and RE. The feedback of the RE is crucial in this step, otherwise the potential cannot be controlled accurately. The subsequent current response arises from the electrochemical reaction occurring at WE. To control the current response, different potential schemes can

be employed. Here two different electrochemical techniques will be described that can be performed in the explained three-electrode configuration. Both cyclic voltammetry and chronoamperometry were used extensively in this project.

2.3.1 Cyclic voltammetry

A typical technique to study the behaviour of electrochemical reactions is cyclic voltammetry (CV). CV involves sweeping the potential between two values back and forth. It is different from linear sweep voltammetry in which the potential is swept forth/back once. Moreover, multiple cycles with different scan rates are performed to study the kinetics of electrochemical reactions. Common scan rates range from 1 to 100 mV/s and usually give different current responses.

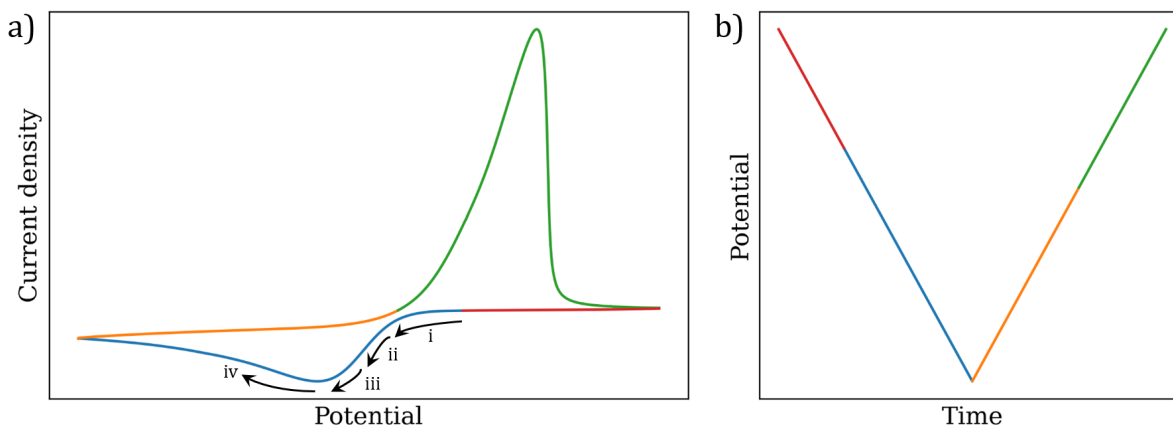


Figure 2.1: (a) Typical cyclic voltammogram in which (i) indicates a non-zero current response upon decreasing the potential, (ii) Butler–Volmer kinetics, (iii) ion depletion and (iv) steady-state approach of the system. (b) The complementary potential scheme. The colours correspond to the forward and backward scan and also change with the sign of the current.

Figure 2.1 shows an illustration of a cyclic voltammogram with an arbitrary scan rate. Two conventions for presenting CV data are in use, but in this thesis solely the IUPAC convention will be shown [18]. This means that upon decreasing the potential (i) a negative current starts to develop, corresponding to cathodic current due to a reduction reaction. After this thermodynamic barrier is exceeded the current response is determined by the kinetics of the reaction [19]. The first part (ii) is governed by Butler-Volmer kinetics, which can be derived from the reaction rate (2.10):

$$v_{net} = k_{ox}c_{red} - k_{red}c_{ox} \quad (2.10)$$

where v_{net} is the net reaction rate and k_{ox} and k_{red} the oxidation and reduction rate constant, respectively.

From the Arrhenius equation (2.11) it follows that the rate depends exponentially on the activation energy, which in this model is assumed to be equal to the Gibbs free energy of the intended reaction.

$$k = Ae^{-E_a/RT} \quad (2.11)$$

where A is a pre-factor and E_a the activation energy.

Subsequently, the Nernst equation can be used to find the equilibrium potential and by using Faraday's law ($J = Fv$) and substituting the formal Nernst (2.5) and Arrhenius (2.11) equation, the formal Butler-Volmer equation (2.12) is obtained:

$$J = nFk^\circ \left(c_{red}e^{f_{ox}(E-E^\circ)} - c_{ox}e^{-f_{red}(E-E^\circ)} \right) \quad (2.12)$$

$$\text{with } f_{red} = \alpha \frac{nF}{RT} \quad \text{and} \quad f_{ox} = 1 - \alpha \frac{nF}{RT} \quad \text{so that} \quad f_{red} + f_{ox} = \frac{nF}{RT}$$

where k° is the standard rate constant at which the system will approach equilibrium and α is the asymmetry factor. This model disregards ion dynamics and from the cyclic voltammogram (Figure 2.1) it can be observed that the current density stops increasing exponentially after a certain potential. Other kinetics start to dominate and these can be divided into processes that occur either in the electrolyte, such as mass and charge transfer, or at the electrode, such as ion adsorption, desorption and conversion.

However, the current density is often only limited due to mass transfer, which can sub-divided into migration, diffusion and convection. Migration is the movement of ions due to a gradient in electrical potential, while diffusion is the movement of species due to a gradient in chemical potential (usually concentration). Convection, on the other hand, occurs when the solvent itself is moving, for instance, when the electrolyte is stirred. All three contribute to the current response simultaneously and a simple mass transfer model is described by the Nernst-Planck equation (2.13):

$$J = \underbrace{\frac{Dze}{k_B T} c E}_{\text{migration}} - \underbrace{D \nabla c}_{\text{diffusion}} + \underbrace{vc}_{\text{convection}} \quad \text{with} \quad E = -\nabla \phi - \frac{\partial A}{\partial t} \quad (2.13)$$

where D is the diffusion coefficient of the reactant, z its valence, e the elementary charge, k_B Boltzmann's constant, E the electric field, ∇c the concentration gradient, v the velocity of the electrolyte, $\nabla \phi$ the electric potential gradient and $\frac{\partial A}{\partial t}$ the change of the magnetic vector potential with respect to time.

When the electrolyte is not stirred, the effect of convection is negligible and only migration and diffusion affect the ion flux towards the electrode. For this reason, the electrical double layer (EDL) gets depleted from ions and grows in size, resulting in a decreasing current decline (iii in Figure 2.1). Hereafter, the current is limited by mass transport from the bulk electrolyte to the EDL, resulting in a decreasing current rise (iv) as the system approaches steady-state at lower potentials. The height of the peak current in between these regimes corresponds to the maximum reaction rate and can be controlled by the scan rate. On the anodic (oxidation) side the current response is similar. However, different kinetics play a role in this example, resulting in an asymmetric voltammogram.*

2.3.2 Chronoamperometry

Next to sweeping the potential such as in CV it is also possible to instantaneously change the potential. This is done with chronoamperometry which is a step voltammetry technique. By keeping the potential constant for a chosen duration a similar current response as in CV is observed. Again, ion depletion and mass transfer limit the current, giving a response equal to the curves in Figure 2.2. Integration of this $I-t$ curve yields the total charge that is transferred to the WE. Using Faraday's law ($Q = nF$) it is then possible to calculate the theoretical conversion of the intended electrochemical reaction and in combination with quantitative characterization the Faradaic efficiency can be computed. The shape of the $I-t$ curve contains information about the kinetics and section 2.5.2 elaborates on several developed models. First, the chronoamperometry technique that was used in this work is discussed, preceded by an introduction to electrocrystallization.

2.4 Electrocrystallization

Extensive theories and models have been developed for the electrocrystallization of metals and usually two stages are distinguished [20–22]. A possible start of the process is shown in Figure 2.3, where nucleation at a defect atom occurs in a 2D fashion. Ions adsorb at the substrate and are converted so that a monoatomic layer of metal is formed. However, if a (detached) metal cluster is in close proximity, instantaneously aggregative (3D) nucleation can take place. Incomplete coverage of the substrate's surface allows this event to reoccur (progressive nucleation) in the next stage. During this growth stage ions/aggregates can be added epitaxially which entails that the preferred crystal orientation is followed.

Three common epitaxial mechanisms are: Volmer–Weber island growth, Frank–van der Merwe layer-by-layer growth and Stranski–Krastanov combined growth [20] (Figure 2.4). Depending on the binding energy and (mis)match between the crystal structures of the metal and the substrate one of these mechanisms is dominant. Moreover, if the binding energy of ions adsorbed on the substrate ($E_{M_{ads}^+ - S}$) is higher than the binding energy of

*Appendix A6 elaborates on models of cyclic voltammetry.

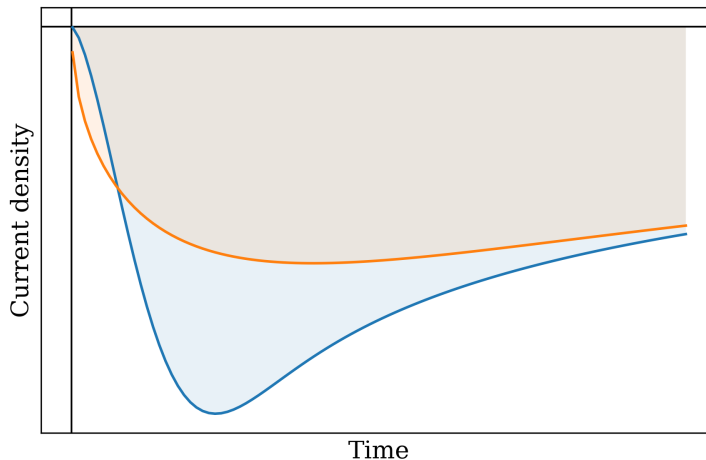


Figure 2.2: Typical chronoamperometry curves in which the area above the curves is a measure for the transferred charge.

ions adsorbed on the metal ($E_{M_{ads}^+ - M}$), it becomes possible to grow at a lower potential than thermodynamically specified. This is called underpotential deposition. In the case of $E_{M_{ads}^+ - S} < E_{M_{ads}^+ - M}$ it is more favourable for ions to attach to the converted metal and an overpotential is needed in order to grow. As the Volmer–Weber mechanism applies to this situation, island formation complicates the growth of a uniform film. In the case of $E_{M_{ads}^+ - S} > E_{M_{ads}^+ - M}$ an underpotential can be used and if the crystallographic mismatch between the metal and the substrate is negligible a film will form layer-by-layer following the Frank–van der Merwe mechanism. However, if the mismatch hampers layer-by-layer growth, the Stranski–Krastanov mechanism is observed, which complicates the formation of thick films.

2.5 Electrochemical deposition of Ag on ITO

In this project ITO is used which has a low surface wettability and, therefore, a standard low $E_{M_{ads}^+ - S}$ [23]. Hence, it is likely that electrodeposition of any metal on ITO follows Volmer–Weber island growth, making a (high) overpotential essential. If chronoamperometry would be performed with a high overpotential, the electrochemical reaction would take place with a high rate. A trade-off under these conditions is that the growth becomes diffusion-limited because of the rapid depletion of ions. Figure 2.5 shows that particles compete due to overlapping depletion layers. The consequence is that particles of different sizes are obtained (increased dispersion) which is disadvantageous for SERS studies and growth of microscale structures. In order to minimize particle size dispersion Scheludko and Todorova introduced

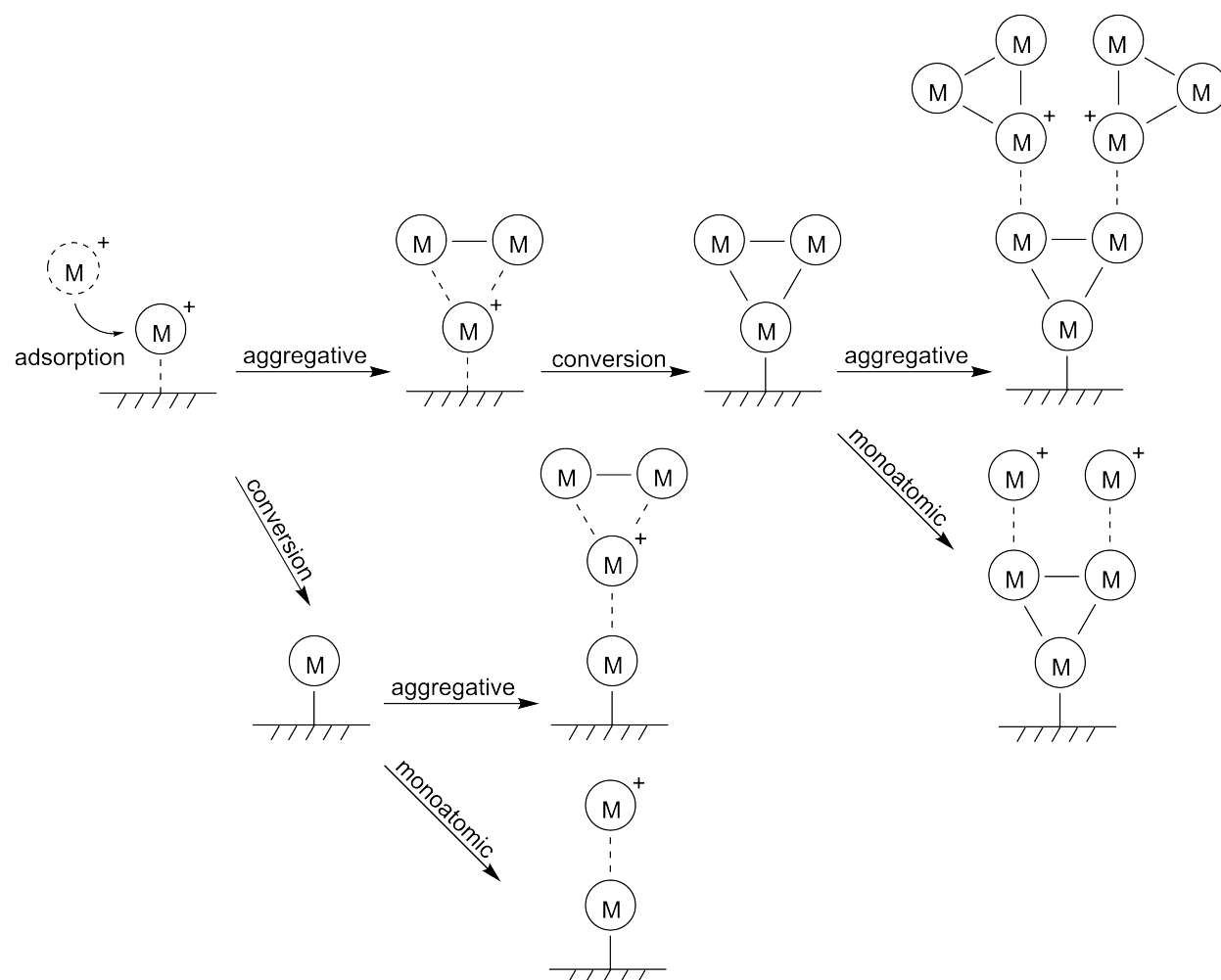


Figure 2.3: Schematic depiction of the monoatomic and aggregative nucleation (left) and its subsequent growth (right) of metal electrocrystallization at one defect atom.

the double-pulse technique [24].

2.5.1 Double-pulse technique

The double-pulse technique involves two subsequent chronoamperometry experiments in which a high overpotential (E_n) is applied for a short amount of time (t_n), followed by a low overpotential (E_g) for a longer amount of time (t_g) (Figure 2.6). In this way, instantaneous nucleation can be ensured while progressive nucleation is prevented. Moreover, by tuning the growth overpotential the rate can be regulated and, if possible, the reaction can be performed under kinetic control. With this technique dimensionally uniform metal particles can be electrodeposited and several successful experiments [14, 26–31] and simula-

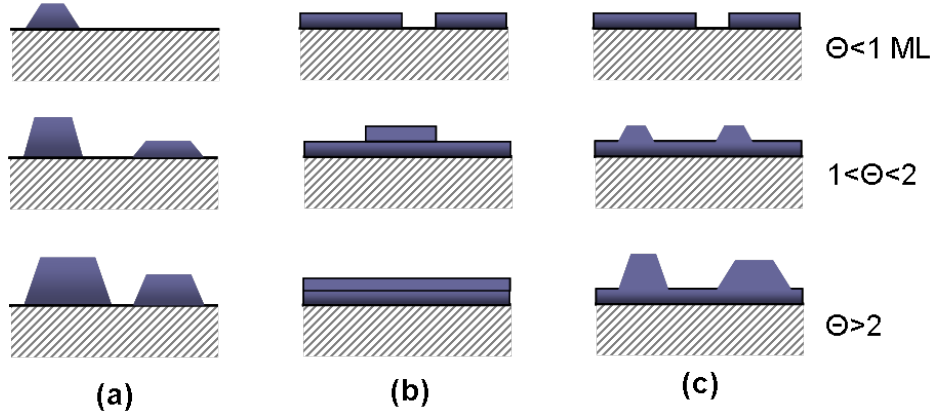


Figure 2.4: (a) Volmer–Weber island growth, (b) Frank–van der Merwe layer-by-layer growth and (c) Stranski–Krastanov combined growth. Θ indicates the coverage and ML stands for monolayer [20].

tions [25, 32] have been reported. Section 5.3 elaborates on the analyses of such experiments and the next paragraph discusses several developed growth models.

2.5.2 Growth models

So far, only irreversible growth has been considered for electrocrystallization of metals. However, nuclei will only survive and grow if they exceed a critical radius r_{crit} [33]. The electrochemical growth of particles follows complex kinetics because of the combination of ion migration and diffusion. Yet, numerous growth models have been developed and this paragraph discusses the field from a bird’s eye view.

In 1903 Cottrell developed an equation that holds his name for diffusion-controlled current response due to an applied potential [34].

$$J = -zFc \left(\frac{D}{\pi t} \right)^{1/2} \quad (2.14)$$

Only planar diffusion was taken into account, however, with the laplace operator other geometries can be computed as well, such as cylindrical or (hemi)spherical diffusion zones. This was done 80 years later by Scharifker and Hills [35, 36], who started studying the effect of overlapping diffusion zones in the cases of both instantaneous and progressive nucleation (2.15). The expressions for non-overlapping hemispherical diffusion zones of nuclei are given by

$$\underbrace{J = -zFc(\pi Dt^*)^{1/2} N_0 k D}_{\text{instantaneous}} \quad \text{and} \quad \underbrace{J = -\frac{2}{3} zFc(\pi Dt^*)^{1/2} AN_0 k Dt^*}_{\text{progressive}} \quad (2.15)$$

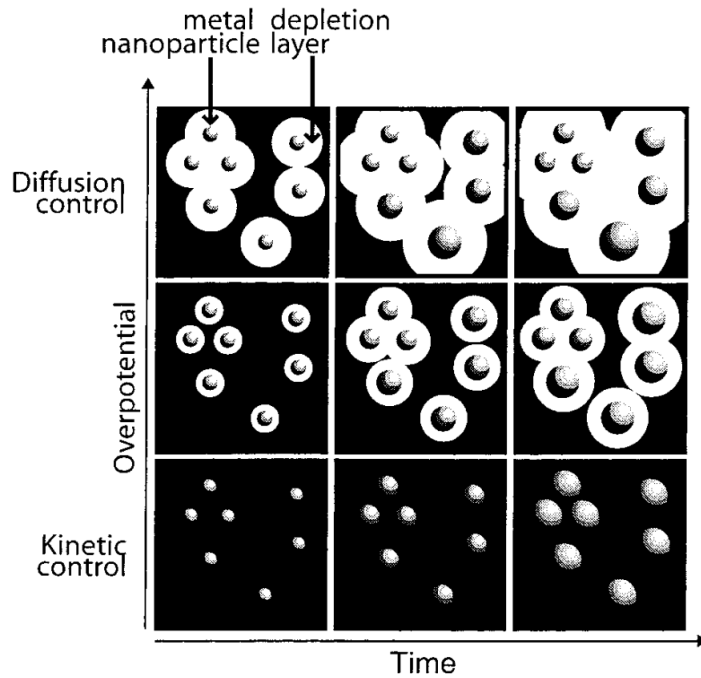


Figure 2.5: Schematic top view of the effect of overpotential and time on the particle size distribution. When depletion layers collide particles become diffusionally coupled and start to compete for ions [25].

$$\text{with } k = \left(\frac{8\pi cM}{\rho} \right)^{1/2}$$

where N_0 is the number of active sites, A the growth rate, M the molar mass and ρ the density of the ionic species and t^* the time. t^* can also be written as $t - t_0$ when there is an induction time (t_0) before the reaction takes place. A complication with rewriting these equations for the situation where diffusion zones do overlap is that nucleation happens on a plane, while growth and diffusion extend into the bulk of the EDL. This poses a $2\frac{1}{2}$ dimensional problem, which cannot be solved within Avrami's theorem[†] for kinetics of crystallizations. Two approaches are feasible: (i) The height h of the hemispheres could be split up in infinitesimal layers with height dh such that 2D diffusion could be computed for each layer separately and integrated to obtain the complete diffusion kinetics. (ii) The hemispheres could be approached by cylinders, such that the problem simplifies to linear 2D diffusion to the hemisphere's/cylinder's projected area. The latter approach was used by

[†]The discussion of Avrami's theorem is beyond the scope of this thesis and interested readers are referred to [37, 38]

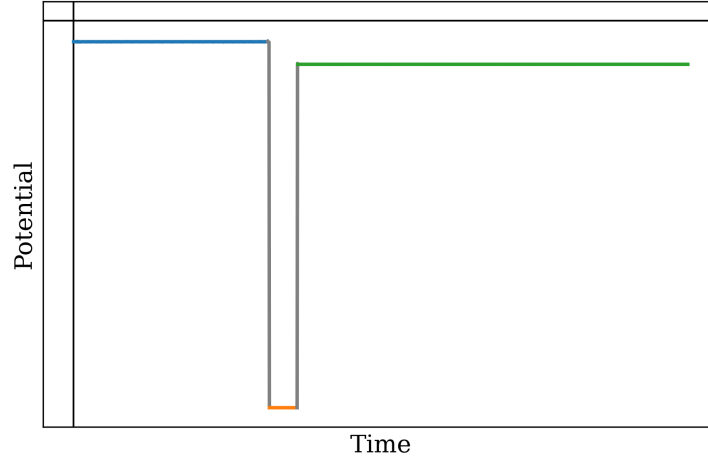


Figure 2.6: Potential scheme of a double-pulse experiment. First the system is stabilized at open circuit potential, then two pulses are applied at high and low overpotential, respectively.

Scharifker and Hills and the Equations in 2.15 can be rewritten into

$$J = \underbrace{-zFc \left(\frac{D}{\pi t^*} \right)^{1/2}}_{\text{instantaneous}} [1 - \exp(-N_0 \pi k D t^*)] \quad (2.16)$$

$$J = \underbrace{-zFc \left(\frac{D}{\pi t^*} \right)^{1/2}}_{\text{progressive}} \left[1 - \exp\left(-\frac{2}{3} A N_0 \pi k D t^{*2}\right) \right] \quad (2.17)$$

In all these 4 equations it is assumed that nuclei irreversibly pass r_{crit} so that the surface ends up in a 'frozen' energetic state and that nuclei grow with a constant rate A : $N(t) = N_0 (1 - e^{-At})$ [39]. However, the number of active sites also decays because of the growth and collision of diffusion zones. In a collaboration between Scharifker and Mostany this is taken into account [40], accompanied with the assumption that this process is faster than the growth of single nuclei. Again approaching the $2\frac{1}{2}$ dimensional problem with equally high cylinders it becomes possible to decouple A and N_0 :

$$J = -zFc \left(\frac{D}{\pi t^*} \right)^{1/2} [1 - \exp(-N_0 \pi k D t^* \theta)] \quad (2.18)$$

$$\theta = 1 - [1 - e^{-At^*} / At^*] \quad (2.19)$$

According to Heerman and Tarallo this model overestimates the diffusion zone expansion as it considers equally high cylinders for all particles, even the ones that have not been born yet in the case of progressive nucleation [41, 42]. They propose that the cylinders can have unequal heights and, therefore, appear and grow at different times during the deposition. This splits the model in an instantaneous and progressive part again and results in the following correction of the model of Scharifker and Mostany:

$$J = \underbrace{-zFc \left(\frac{D}{\pi t^*}\right)^{1/2} \frac{1}{\theta} [1 - \exp(-N_0\pi kDt^*\theta)]}_{\text{instantaneous}} \quad (2.20)$$

$$J = \underbrace{-\frac{2}{3}zFc \left(\frac{D}{\pi t^*}\right)^{1/2} \frac{At^*}{\theta} [1 - \exp(-N_0\pi kDt^*\theta)]}_{\text{progressive}} \quad (2.21)$$

This chapter elaborates on the experimental details for the electrodeposition of Ag on ITO. The sample and electrolyte preparation are discussed, followed by descriptions of handling the electrochemical cell and a typical experiment.

3.1 Sample preparation

Poly-crystalline ITO-coated glass (180 nm ITO on 1.1 mm glass) was obtained from KinTec in sheets of 15x15 cm. These sheets were put on a transparent sticker and cut with a disk saw in pieces of 25x25 mm such that 36 pieces per sheet were obtained. After detaching the samples from the sticker they were wiped with deionized water and soap, and brushed with ethanol using a toothbrush to remove eventual sticker residue. Subsequently, the samples were placed in a Teflon holder (Figure 3.1) and sonicated for 10 min in ethanol, 10 min in acetone and 5 min in isopropanol. In between the sonication steps the samples were dried with a N₂ gun. Although the samples were stored in a desiccator, it was decided to perform this part of the cleaning no earlier than 2 weeks before deposition experiments. Right before an experiment, however, O₃ cleaning was performed to remove any remaining organics. The UV/Ozone ProCleaner (BioForce Nanosciences) uses ultraviolet light to convert O₂ into O₃ via the well-known photodissociation mechanism [43]. The samples were exposed to this O₃ environment for 15 min before being used.

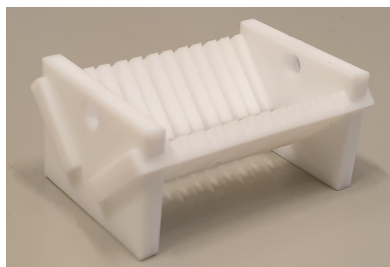


Figure 3.1: Teflon holder for 6 ITO samples that was used during cleaning.

3.2 Electrolyte preparation

Deionized water was further purified using a Millipore Simplicity[®] system ($\rho > 18.2 \text{ M}\Omega\text{cm}$) and 25 mL was added to a 50 mL volumetric flask. 710.2 mg of Na_2SO_4 (Sigma-Aldrich, >99% purity) was dissolved by swirling the solution. This was repeated with 9.2 mg saccharin (Sigma-Aldrich, >99% purity) and after the addition of 15.6 mg of Ag_2SO_4 (Sigma-Aldrich, >99% purity) the solution was sonicated for 3 min to dissolve remaining salts. 1.9 mmol H_2SO_4 (Acros Organics, 96 w% in H_2O) was added and the volumetric flask was filled up to 50 mL with more Milli-Q water so that the final concentrations correspond to: 100 mM Na_2SO_4 , 1 mM Ag_2SO_4 , 1 mM saccharine and a pH of 1.7 [31]. The latter was checked with a Hanna Piccolo pH meter (Sigma-Aldrich).

3.3 Electrochemical cell

The electrochemical cell used in this project is designed and built in-house and in Figure 3.2 a and b a picture and a drawing of its cross section are shown, respectively. The cell is made of polyether ether ketone (PEEK) in order to withstand (highly) acidic or alkaline electrolytes. It is designed in such a way that the 25x25 mm samples can be placed on top of 4 contact points and locked in place by screwing a holder into the cell when it is upside down. Contacting the working electrode at 4 points ensures a more uniform charge density opposed to contacting at 1 point.* In the middle, the sample is pressed against a viton O-ring, leaving an area of 95.03 mm^2 exposed to the inner chamber of the cell. On the other side of the chamber a Pt disk with an area of 307.9 mm^2 acts as a counter electrode. Remember that the area of the counter electrode has to be larger than that of the working electrode in order not to limit the reaction with charge transport kinetics. Next to that, Pt is used because of its inertness and good performance as electrocatalyst [44]. On the sides of the chambers in- and outlet valves are present and also a reference electrode can be inserted to perform three-electrode configuration experiments.

In this project the same leakless ET072-1 micro Ag/AgCl electrode is used. However, Appendix A1 shows that these reference electrodes deviate from the actual Ag/AgCl potential and this gets worse with time. Therefore, the potential of this reference electrode was measured on each day with experiments against a radiometer analytical XR300 Ag/AgCl reference electrode. This electrode was stored in a saturated KCl/AgCl solution and only used to measure the potentials of micro electrodes to minimize its deterioration. To do this, both electrodes were submerged in 1 M Na_2SO_4 and connected in a two-electrode configuration in which the micro electrode acts as the working electrode and the reference electrode as the counter electrode. By measuring the open circuit potential of this system for 10 min, the deviation of the micro electrode from the reference electrode can be determined accurately.

*1-point depositions resulted in lower current responses and depositions of bad quality (see Appendix A2)

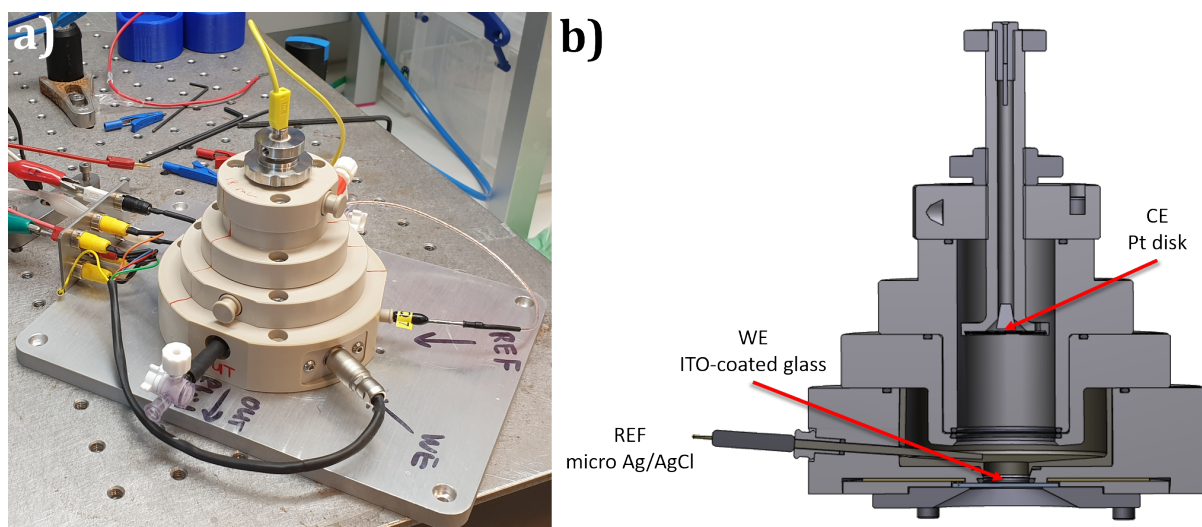


Figure 3.2: (a) Picture of the home built electrochemical cell in which the yellow wire on the top connects the counter electrode to the potentiostat. (b) Schematic drawing of the cell.

This value can then be used to correct the potential in the subsequent experiment(s). When the micro electrode was not in use, it was stored in Milli-Q water.

The majority of the experiments was performed with a SP-300 potentiostat from Biologic, which can be operated using software from EC-Lab. However, apart from parameters falling within the specifications of the potentiostat, the software gave ambiguous feedback from time to time. Appendix A3 elaborates on this lack of performance and provides compromises that have been made in order to conduct valid experiments.

3.4 Typical experiment

Before using a new electrolyte in the cell it was filled with 1 M H_2SO_4 and left to soak overnight.** After this the cell was rinsed with Milli-Q water for 3 times and dried extensively with a N_2 gun. The potential of the micro reference electrode was measured and together with a freshly cleaned sample it was mounted on the cell. Via one of the valves electrolyte was added with a syringe until it would come out of an air hole situated above the other valve, which indicates that all three electrodes are touching the electrolyte. By turning the cell upside down and looking through the sample it was checked if there were no air bubbles trapped in the chamber. Subsequently, the electrodes were connected to the potentiostat, the preferred parameters were entered in the software and the experiment was run using parameters that are specified in Appendix A4. Afterwards, the electrodes were readily disconnected to prevent charge from flowing back. The sample was removed, dipped in

**When using an electrolyte of the same consistency this step was skipped

Milli-Q water, dipped in isopropanol, and dried with a N₂ gun. The electrolyte was removed from the cell with a syringe and the cell was flushed 2 times before being stored, filled with Milli-Q water.

In order to characterize the electrodeposited material several characterization techniques have been employed. A scanning electron microscope (SEM) has been used to get information about the morphology of the surface while the topography of the surface was mapped with atomic force microscopy (AFM). Energy-dispersive X-ray spectroscopy (EDX) gave insights into the elemental composition of the samples. The crystal orientation of the ITO from each substrate was elucidated with X-ray diffraction spectroscopy (XRD).

4.1 Scanning Electron Microscopy

Rather than conventional microscopes that use photons to compose an image, a SEM detects electrons to create an image [45]. First, electrons are generated with an electron gun via either thermionic or field-generated emission. In the former case a metallic filament is heated to high temperatures such that it starts emitting electrons. A typical example is tungsten, which should be heated to 2200°C to emit a useful amount of electrons. Straightforwardly, this should be done under high vacuum (10^{-3} – 10^{-7} mbar) to prevent the electrons from interacting with molecules in the air. In the design of field-generated emission even ultra high vacuum (10^{-7} – 10^{-12} mbar) is necessary to facilitate the extraction of electrons from the filament by a strong electric field. Subsequently, these electrons are focused and accelerated in a beam using electromagnetic lenses, which is then scanned in a raster across the exposed area. The electrons in this beam reach energies of 5–10 keV before they hit the sample. Upon doing so, the electrons from the beam interact with the electrons from the material such that several signals exit the sample, summarized in Figure 4.1.

In this work we are interested in the secondary electrons, which are created when an electron from the beam hits a loosely bound electron from an atom in the sample (outer shells). This electron is then ejected with an energy of 1–15 eV, which is just enough to travel a few nm through the material. Therefore, only secondary electrons from the surface leave the sample, giving topographic information when detected. A FEI Verios460 SEM was used, which has two detectors for secondary electrons. The Everhart–Thornley detector (ETD) is located next to the sample stage and by applying a positive potential it attracts electrons. Here the electrons hit a scintillator which contains a materials that luminesces when struck by electrons. After enhancement of the signal with a photomultiplier tube it is displayed on a monitor. The through the lens detector (TLD) is located in the beam path.

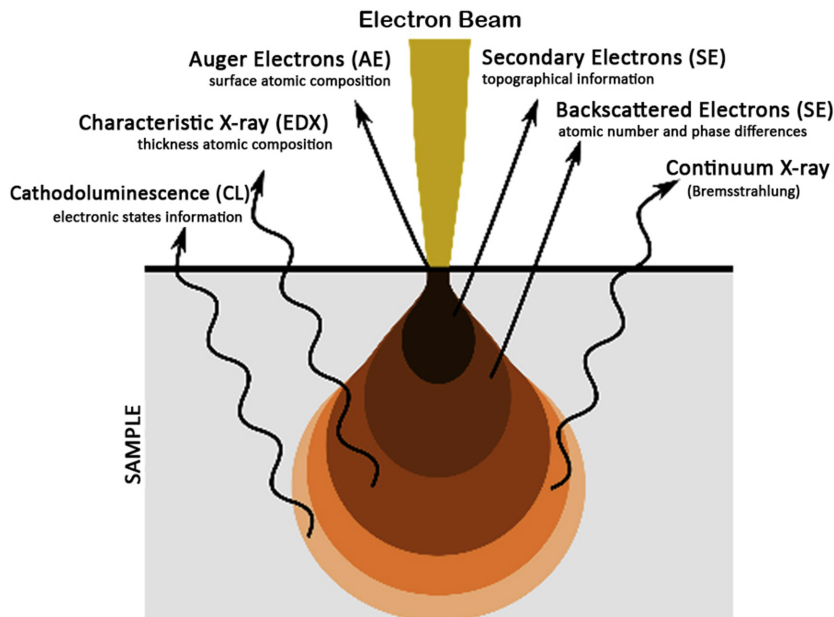


Figure 4.1: Signals exiting a sample after exposure with a focused electron beam [46].

Therefore, it will nearly not detect electrons that have interacted with their environment after ejection, which allows for ultra high resolution imaging. In this setup it is possible to actively switch from detector, such that coarse focusing can be performed with the ETD and fine focusing with the TLD. Navigation on the sample is facilitated with a NavCam system.

4.2 Energy-Dispersive X-ray spectroscopy

Another signal that leaves the material after exposure with the focused electron beam consists of X-rays. These are formed when an electron from the beam bumps into a more tightly bound electron from an atom in the sample (inner shells). To fill up this 'gap' an electron from a higher shell is transferred, which causes a photon to be ejected. Since these photons have energies in the keV regime they can travel through (a large part of) the sample. Besides that, the energy of such photons depends on the energy spacing of the shells and since this is different for each element these photons have characteristic energies. By using an energy-dispersive spectrometer the bulk signal can be split up per element for which the peak height is an indication of the abundance in the sample. The absolute intensity, however, is determined by the amount and energy of electrons in the beam and the element dependent interaction cross-section. Disadvantages of increasing these are that the beam might destroy the sample and that more background signal is observed due to a continuous X-ray ejection called brehmsstrahlung. The key of this technique is to balance the signal-to-noise ratio.

4.3 X-ray Diffraction spectroscopy

In this technique the sample is illuminated with X-rays under an angle. Crystalline regions in the sample will diffract these X-rays so that the angle of incoming X-rays is different than that of the angle of outgoing X-rays. The angle of diffraction is related to the distance between the planes of the crystal lattice via Bragg's law $n\lambda = 2d \sin \theta$, where n is the order of diffraction, λ the wavelength of the used X-rays, d the distance between the planes and θ the angle of diffraction. Depending on the monochromaticity of the source sharp peaks can be obtained from which the intensity is a measure of the abundance of that crystal orientation. In this work a machine was used that produces Cu K_α and K_β radiation with wavelengths of 1.54184 and 1.39222 Å, respectively.

4.4 Atomic Force Microscopy

AFM is based on the interaction of the substrate with a sharp tip that is attached to a cantilever. By scanning this probe across the surface, a map of this interaction is made. Depending on what external parameters are varied or kept constant for either the tip or the substrate, different interactions can be measured. This project is concerned with the topography of the substrate, which can be easily obtained by measuring the van der Waals interactions. The only parameter that has to be controlled and monitored is the distance between the tip and the substrate. Two well-known AFM setups are available to do this: contact mode and tapping mode.

In contact mode the tip is touching the surface and upon doing so the cantilever is deflected because of van der Waals forces. This deflection is monitored with a laser that is reflected by the top of the cantilever. By locking the deflection the system tries to keep the force on the substrate constant. Therefore, the cantilever has to move up and down when encountering a topographic slope. This is done with a piezo motor, which is able to accurately track the height movements. A disadvantage of this mode is that there is constant contact between sample and tip, increasing the chance of damaging of both. This issue can be resolved with the tapping mode setup in which the cantilever is mechanically oscillated at its resonance frequency. Now the cantilever moves by locking the amplitude of this oscillation and the tip is no longer in contact with the sample (provoking damage). Samples with high roughness, however, can induce large errors in the oscillation amplitude as no longer an absolute force is measured. Therefore, this work used a combination of both modes which is available in Bruker's PeakForce tapping AFM. The ScanAsyst software was used because of its automatized and dynamic settings for the feedback loop [47].

This chapter discusses the results that were obtained by using the double-pulse technique for the electrodeposition of Ag on ITO. First, the characterization of the substrate by XRD is discussed, followed by the determination of electrolyte and its electrochemical parameters by CV. Then, the results from sweeping such an electrochemical parameter are discussed for which a particle analysis method from SEM data is used. Complementary, the results from chronoamperometry analysis and modeling are shown to shine a light on the nucleation mechanism. Finally, conclusions on the growth mechanism are drawn using AFM.

5.1 ITO characterization

(Sandmann et al., Hau et al. and Ueda et al.) have shown that it is difficult to form a continuous film of Ag on ITO by electrodeposition. To investigate the effect of the preferred crystal orientation, XRD spectroscopy on samples from two different ITO batches was performed. The difference in XRD peaks is shown in Figure 5.1 and Appendix A5 gives an overview of the peak height ratios that can be calculated from these spectra. It becomes clear that ITO samples from batch 2 (MD210412_B in Figure 5.1) have a preferred orientation towards the (222) plane, while the ratio of the peak height between the (222) and (400) plane of batch 1 (MD210324_A) is more or less equal. This difference in polycrystalline orientation could have an effect on the surface potential and, therefore, the ease and mechanism of deposition.

5.2 The choice of electrolyte

Next to studying the deposition mechanism, an effort was made to use a cyanide-free alternative to conventional electrolytes [5, 6]. Kung et al. used both the commercially available Clean Earth electrolyte and the saccharin-based electrolyte to deposit Ag on Ni. In this project the Clean Earth electrolyte was used as benchmark because of its substrate independent performance. However, it is likely that the Clean Earth solution contains numerous organic additives, which makes studying the deposition mechanism and modeling chronoamperometry experiments performed with this electrolyte difficult. The saccharin-based electrolyte described in section 3.2, on the other hand, contains only one organic additive that is expected to form an organometallic complex with Ag [48], namely saccharin.

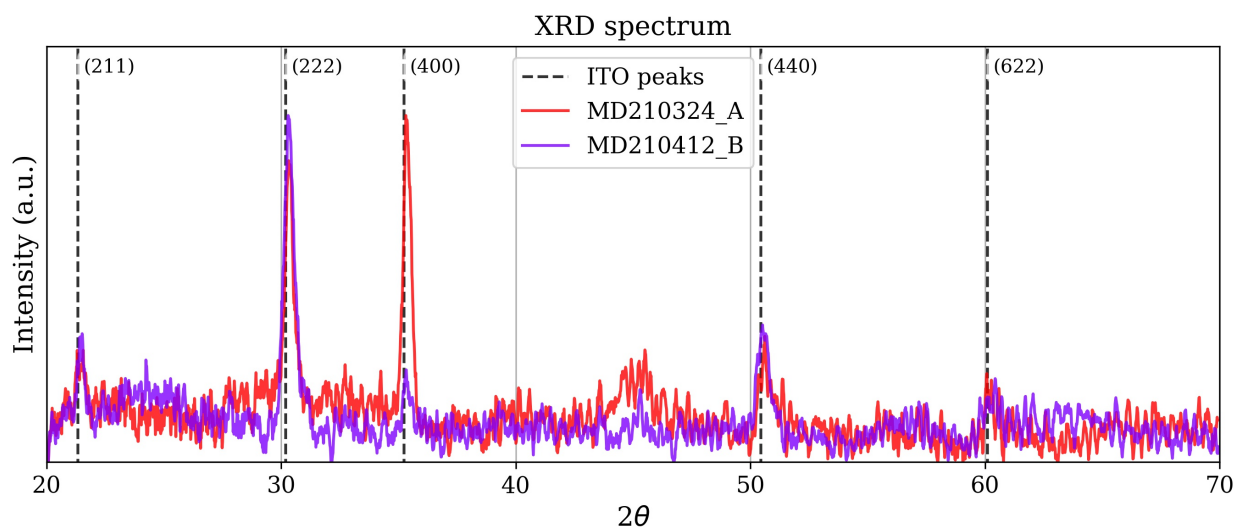


Figure 5.1: XRD spectra from two ITO samples from different batches.

A preliminary performance comparison can be made with cyclic voltammetry as the current response is a measure for the rate of the electrochemical reactions taking place. Figure 5.2 shows cyclic voltammograms (CVs) for the Clean Earth electrolyte and the homemade electrolyte, with and without saccharin. All three electrolytes show a cross-over in the reduction regime, which is most pronounced for the electrolyte without saccharin. This cross-over could be explained by an increase of active area after the forward scan as readily deposited Ag increases the surface area. The peak currents for the Clean Earth electrolyte are clearly higher, which indicates that a higher reaction rate could be obtained. Several models have been developed to extract the reaction constant and even the diffusion constant of the ionic species from cyclic voltammetry measurements [49–51]. Appendix A6 elaborates on these and shows examples of calculations for the Clean Earth electrolyte.

The shift in potential for the CV indicates that the electrolytes exhibit different thermodynamics, while the relative range in which the electrochemical reactions takes place is equal. From these reduction and oxidation ranges one can estimate what potentials should be used for electrodeposition. For example, Kung et al. used the following electrochemical parameters for the saccharin-based electrolyte: $t_n = 10$ ms, $E_n = 0.143$ V vs. Ag/AgCl, $t_g = 50 - 400$ s and $E_g = 0.373$ V vs. Ag/AgCl. Comparing these values with the CV it is observed that E_n would be a relatively high overpotential (lower absolute potential) to perform the reduction on ITO, while E_g would be a moderate overpotential. Moreover, the duration of the first pulse could not be obtained because of the potentiostat performance (Appendix A3). Therefore, a minimum of $t_n = 30$ ms was used in this project. The duration of the second pulse was important for the analysis of the samples after chronoamperometry as it determines the size of the particles [30]. To be able to analyze these particles with SEM

it was decided to use $t_g = 20$ s as preliminary experiments showed that $t_g = 5$ s was too short to obtain 'visible' particles (likely due to not reaching r_{crit}). The next section discusses the analysis of the samples using SEM.

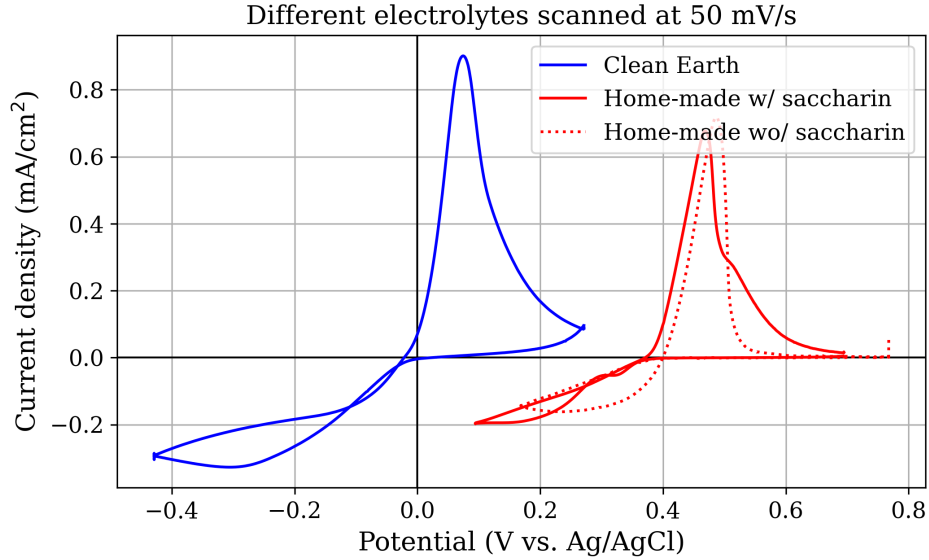


Figure 5.2: Cyclic voltammograms of three different electrolytes scanned at 50 mV/s.

5.3 Particle analysis

Now that the electrochemical barriers have been identified, it is interesting to sweep electrochemical parameters such that the mechanisms of electrodeposition of Ag on ITO can be investigated. To analyze the results of these double-pulse experiments SEM was used. In Figure 5.3 it can be observed that nanosized Ag particles are obtained with the saccharin-based electrolyte. By analyzing these pictures with ImageJ according to Appendix A7 the following quantities can be extracted:

$$\text{Particle density: } \rho = \frac{N}{A} \quad (5.1)$$

$$\text{Surface coverage: } \theta = \frac{\sum p_A}{A} \quad (5.2)$$

where N is the number of particles, A the total surface area and p_A the area per particle such that the sum is the total particle area. To account for eventual inhomogeneity across the samples, 6 images per sample were saved: 2 from the center, off-center and edge, respectively.

By combining these parameters from each image, representative quantities for each sample with a certain standard deviation can be found. In addition, particle size distributions can be obtained and by approaching the particles with hemispheres (so that the projected area $A = \pi r^2$) their abundance and size can be linked to the deposition mechanisms described in Chapter 2. Figure 5.3 clearly shows that E_n affects the particle density. Therefore, E_n was varied over a broad range and the next section discusses the quantities that were extracted from the SEM images of these experiments.

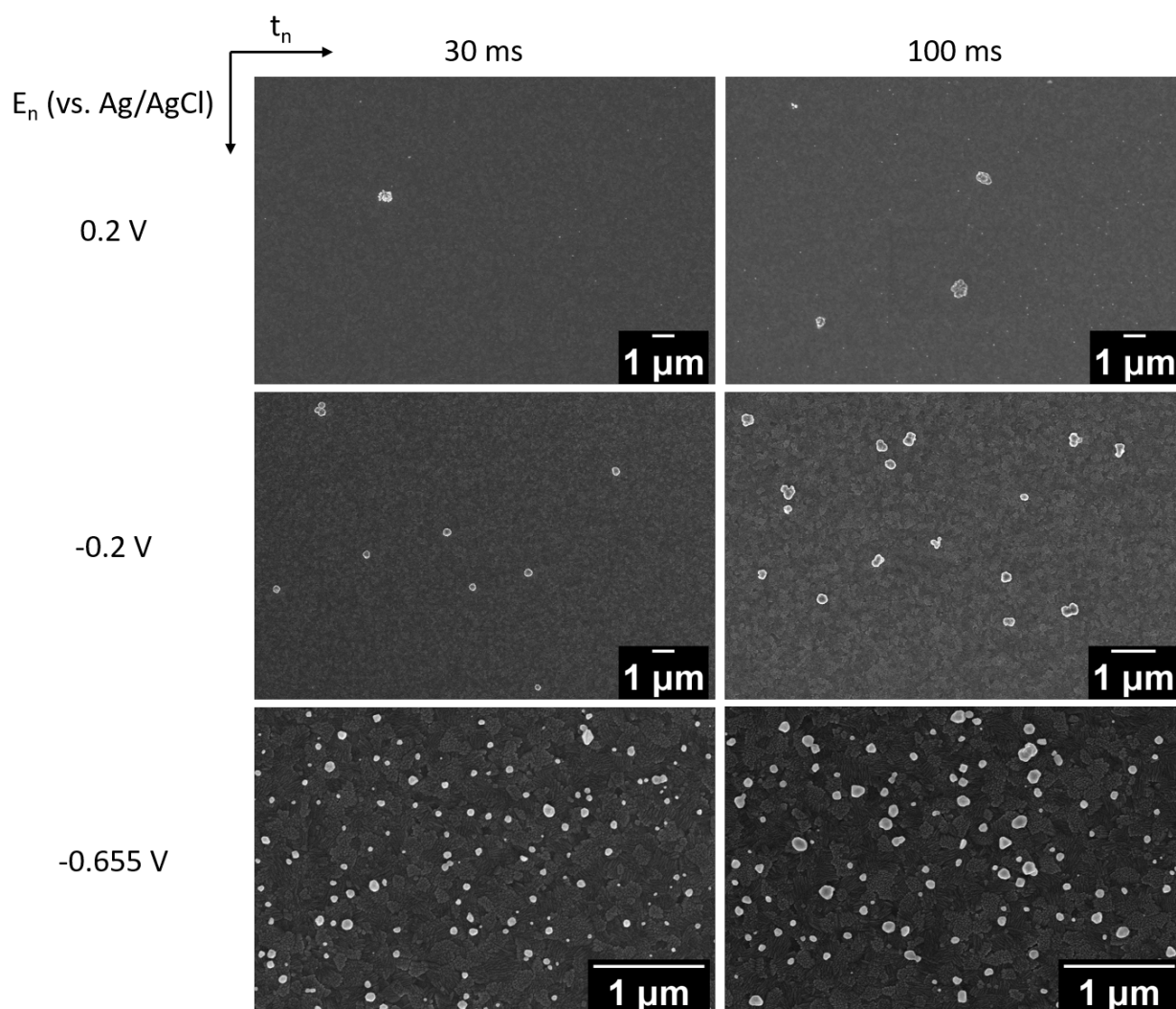


Figure 5.3: SEM images of electrodepositions of Ag on ITO using different E_n and t_n . The particle density for these samples can be found in Appendix A2

5.4 The effect of E_n – saccharin-based electrolyte

To study the effect of the preferred orientation of ITO, E_n was swept for samples from two different batches. Figure 5.4 shows the particle density versus the nucleation potential and it is observed that towards higher overpotentials also higher particle densities are obtained for both batches. This is expected as increasing E_n results in higher reaction rates (Equation 2.11). The average particle size, however, decreases and this is shown for batch 1 in Figure 5.5. These violin plots demonstrate the particle size distribution and should be interpreted as smoothed histograms. In an extreme case of diffusional coupling one would observe two distributions, namely that of smaller and larger particles. Nevertheless, this has not been observed yet [14, 15, 30], and also Figure 5.5 does not show a significant change in distribution shape.

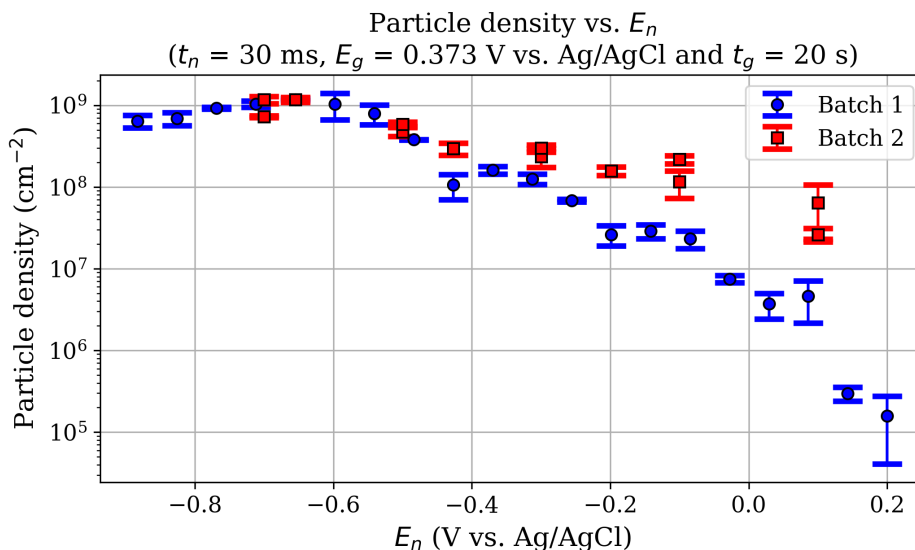


Figure 5.4: Particle density versus the nucleation potential for both ITO batches.

The surface coverage depends on both the particle density and the particle size. Figure 5.6 shows that the surface coverage follows the same trend of the particle density, indicating that under these electrochemical conditions the particle density defines the surface coverage rather than the particle size. In addition, it is remarkable that for both batches a plateau is reached below -0.65 V in both the surface coverage and particle density plots. This could be explained by the interplay of E_n and t_n as the latter should be short enough to prevent diffusional coupling and/or fractal island growth [52]. It is likely that at $E_n < -0.65$ V the nucleation rate is so high that diffusional coupling can not be prevented within 30 ms. Therefore, particles that nucleate too close to each other will not survive in the subsequent growth step and this could lead to a decrease in particle density, which is slightly observed.

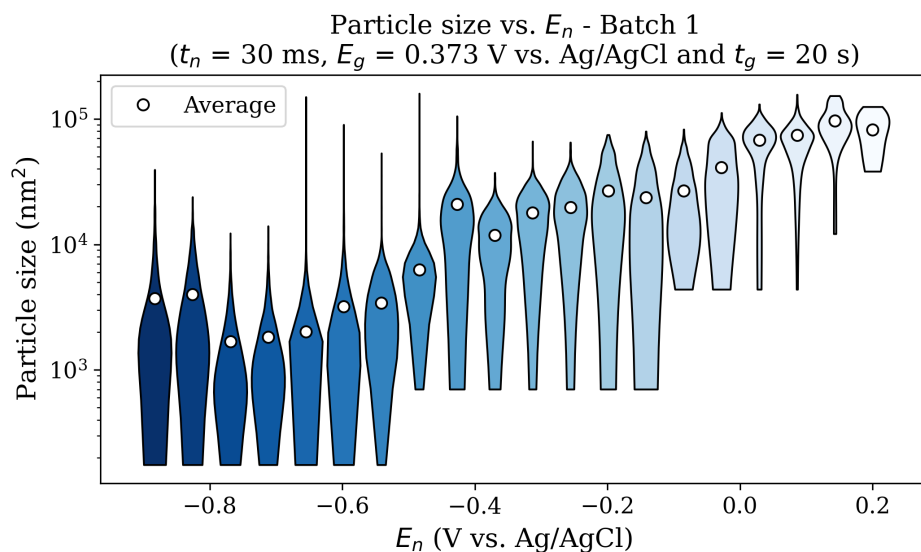


Figure 5.5: Violin plots of the particle size distributions from experiments with different overpotentials from batch 1.

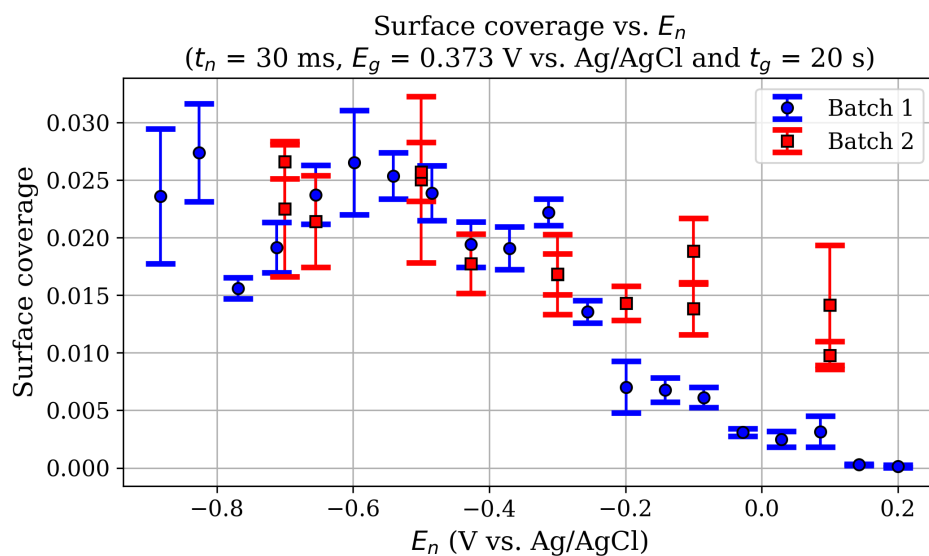


Figure 5.6: Surface coverage versus the nucleation potential for both ITO batches.

Finally, from these plots it becomes clear that the ITO batches follow different mechanisms above -0.4 V and to investigate this further the particles are approached by hemispheres such that the radii of particles can be calculated.

Figure 5.7 shows that the mean radius starts to deviate for both batches above -0.4 V as well. The error bars indicate the absolute standard deviation (σ_{abs}) and according to Ueda et al. the slope of σ_{abs} versus the swept electrochemical parameter gives a preliminary indication for the mechanism. From the trends in Figure 5.8 it becomes clear that the batches indeed follow different mechanisms. However, to determine the extent of diffusional coupling, and therefore progressive nucleation, σ_{abs} should be plotted against the mean radius. Such a plot contains time-dependent information that cannot be envisioned with certainty by only sweeping the overpotential. Unfortunately, no experiments were performed with the saccharin-based electrolyte in which the overpotential was kept constant and the growth time was varied.* Therefore, it remains unclear what mechanisms result in different particle density and surface coverage from the particle analysis.

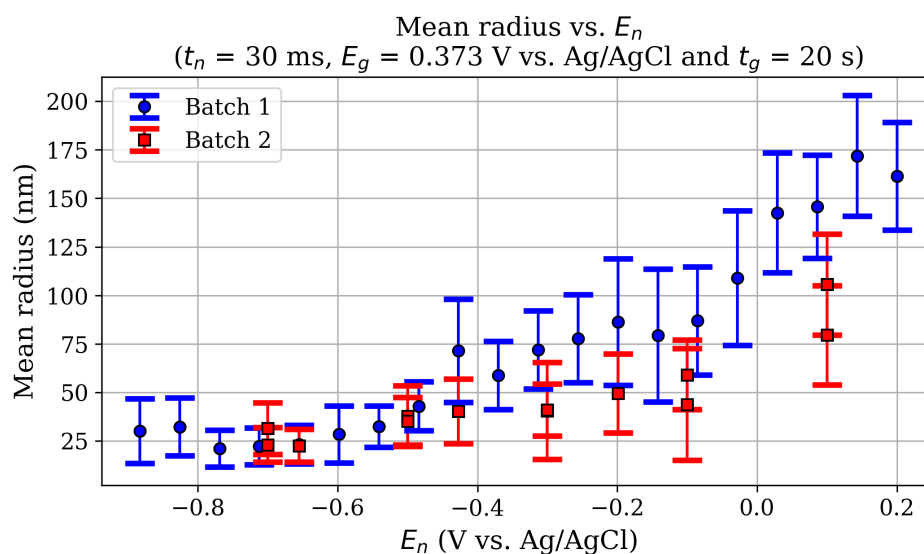


Figure 5.7: Mean radius with absolute standard deviation (σ_{abs}) as error bars versus the nucleation potential for both ITO batches.

*This was done for the Clean Earth electrolyte and a short discussion can be found in Appendix A2, accompanied with a summary of other electrochemical parameters that have been investigated.

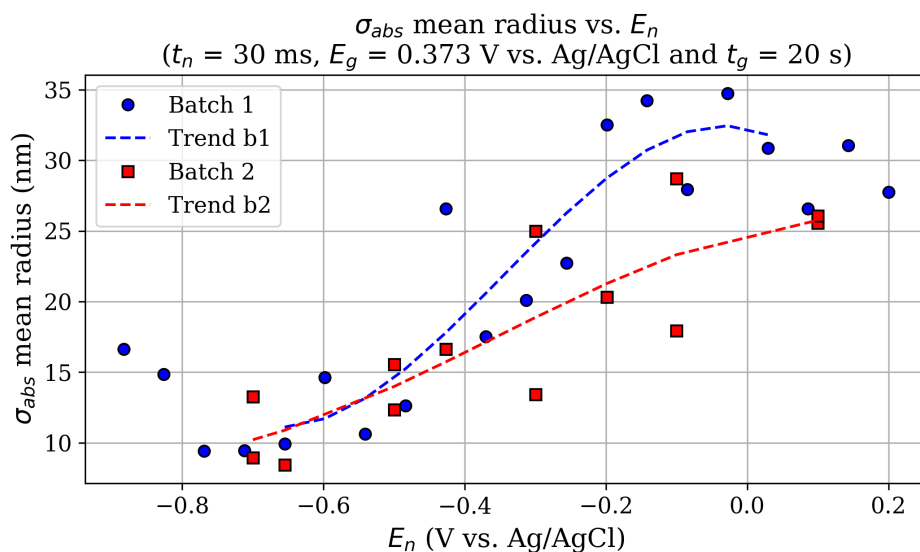


Figure 5.8: Absolute standard deviation (σ_{abs}) of the mean radius with trends versus the nucleation potential for both ITO batches.

5.5 Chronoamperometry analysis

Next to the particle analyses, chronoamperometry data may also yield useful information about the nucleation/growth mechanism of an experiment. Section 2.5.2 showed that several models have been developed to fit single-pulse chronoamperometry experiments. In this work, however, the double-pulse technique has been used, which makes it questionable to use the same models for fitting the data. In order to minimize this discrepancy the concept of induction time was introduced in each model, which allows current to start flowing at later times t than $t = 0$. Moreover, this adaptation turned out to be necessary to obtain reasonable to good fits for the part of the $I - t$ curves after the nucleation pulse.

The goal of finding an appropriate model is to balance simplicity and goodness of the fit. The models in section 2.5.2 increase in complexity, which implies that ideally a model of Scharifker and Hills should be used. Their first description excludes the overlap of diffusion zones, which is not realistic in these experiments. Therefore, their second description was used (Equations 2.16 and 2.17) in which the hemispherical diffusion zones are approached by cylinders and the growth rate A is coupled to the number of active sites N_0 in the case of progressive nucleation. Other parameters, such as concentration c and diffusion coefficient D , can be fixed, but they are not known exactly as it is expected that saccharin forms a complex with Ag [48]. Yet, the ion that is converted is Ag^+ , so the molar mass M and the density ρ are known. t_0 varies slightly between experiments as the limits of the potentiostat were approached (Appendix A3). Summarized, c , D and t_0 were fitted within tight boundaries,

while initial guesses for N_0 and AN_0 were swept over several orders to prevent the model from ending up in local minima.[†]

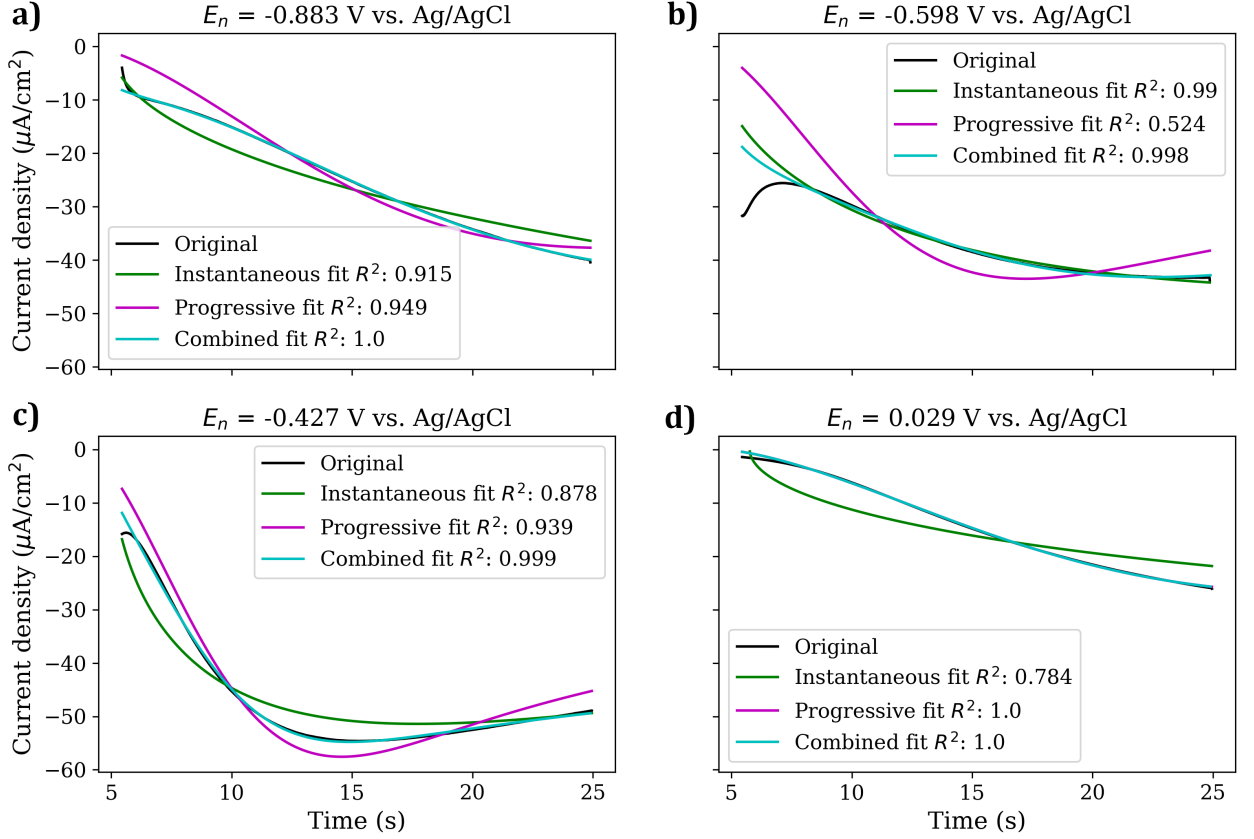


Figure 5.9: Fits of the models described in Equations 2.16, 2.17 and 5.4 for chronoamperometry curves after 5 s at OCP and a nucleation pulse of 30 ms.

To compare the goodness of fits the well-known R^2 -value is used which is defined by

$$R^2 = 1 - \frac{\sum (J_i - J_f)^2}{\sum (J_i - \bar{J}_i)^2} \quad (5.3)$$

where J_i is the original data, J_f the fitted data and \bar{J}_i the mean of the original data. Figure 5.9 shows fits for both the instantaneous and progressive model for chronoamperometry data from experiments with four different E_n for batch 1, while Figure 5.10 shows the R^2 values of these fits for the whole E_n range. The trends indicate that at high potentials the growth is progressive as the R^2 of the progressive fit is closer to 1 than that of the

[†]The Python script that was used to perform these fits is available on request.

instantaneous fit (Figure 5.9 d). Decreasing the potential (higher overpotential) below -0.4 V, however, switches the growth behaviour from progressive to instantaneous (b). This could explain the difference in particle size and density between batch 1 and 2 above -0.4 V. Upon decreasing the potential beyond -0.6 V the growth starts to become more progressive again, according to trend 2 in Figure 5.10. This might explain the hampered increase in particle density as diffusion-limited growth starts to take over. To confirm the switching of models with potential, a combined version of the models was fitted to the data (Equation 5.4) that follows from a simple addition.

$$J = -zFc \left(\frac{D}{\pi t^*} \right)^{1/2} \left[1 - \underbrace{\alpha \exp(-N_0 \pi k D t^*)}_{\text{instantaneous}} - (1 - \alpha) \underbrace{\exp\left(-\frac{2}{3} A N_0 \pi k D t^{*2}\right)}_{\text{progressive}} \right] \quad (5.4)$$

where α is bound to be between 0 and 1 and indicates the weight of both models in the fit. Also the shape of these fits at four E_n have been shown in Figure 5.9.

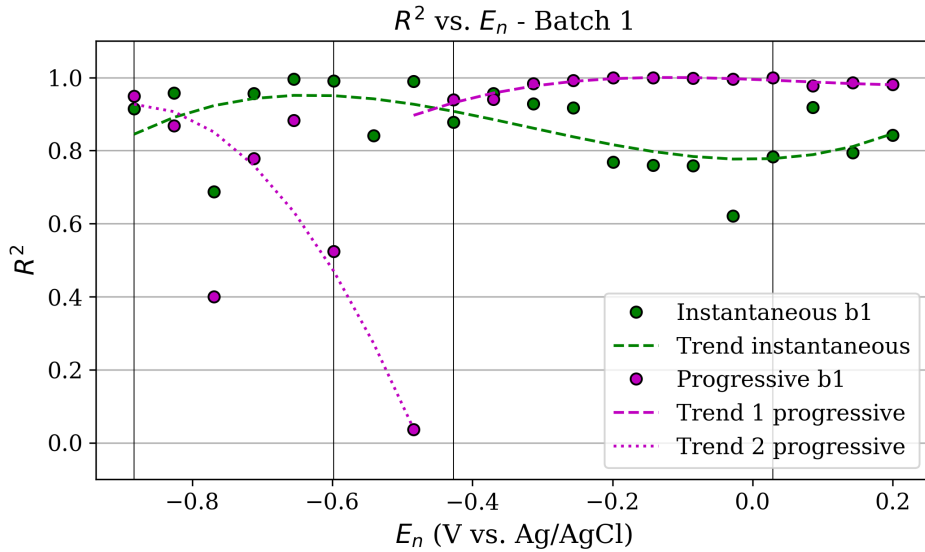


Figure 5.10: R^2 versus the nucleation potential for ITO samples from batch 1. The dashed and dotted lines indicate the identified trends and serve as a guide for the eye. The vertical lines indicate the potentials for which the fits were shown in Figure 5.9.

Since the difference between both parts is a factor $\frac{2}{3} A t^*$ in the exponent and A is not present in the instantaneous part of this model, it is expected that α becomes unpredictable when instantaneous behaviour dominates. This is clearly shown for batch 2 in Figure 5.11, which shows no trend for α along the potential range. This supports the expectation from

the particle analysis that batch 2 shows no change in nucleation mechanism. For batch 1, however, two trends can be observed when the potential is decreased. First, α shows an increase in the reliable regime $0 < \alpha < 0.5$, such that the nucleation mechanism becomes less progressive down to -0.4 V. Then α decreases again, indicating that the nucleation mechanism becomes more progressive. Apart from the absence of a trendless region, the combined fits could explain the switching behaviour deduced from the individual fits. To complete this study, it is necessary to perform experiments with batch 2 at higher overpotentials as it is expected that the particle density can be increased even more before encountering progressive nucleation.

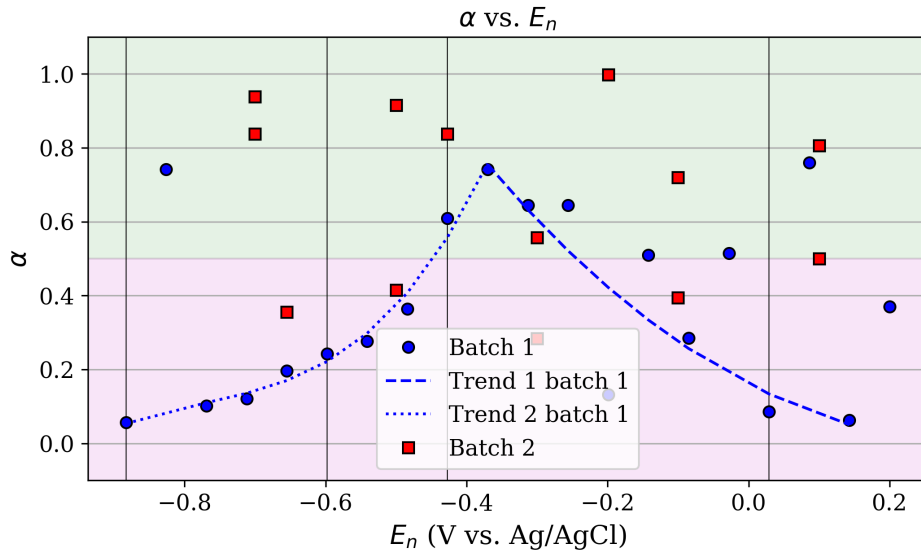


Figure 5.11: α versus the nucleation potential for both ITO batches. The dotted line indicates the increasing α trend for batch 1, while the dashed line indicates the decreasing trend. Values >0.5 indicate instantaneous behaviour (green), while values <0.5 indicate progressive behaviour (magenta). The vertical lines indicate the potentials for which the fits were shown in Figure 5.9.

5.6 Growth analysis

So far, the particles were approached by hemispheres with a constant radius. In this scenario the in- and out-of-plane growth rates are equal, resulting in a $y = ax^{3/2}$ correlation for the volume ($\frac{2}{3}\pi r^3$) and projected area (πr^2). To visualize this one can use a log-log plot in which a straight line is obtained with a slope of 1.5. If the slope deviates from this, either in- (slope < 1.5) or out-of-plane (slope > 1.5) growth is more prominent. By analyzing the samples from both batches with AFM the prominent growth direction in the first 5 s was identified.

Figure 5.12 shows that the growth on both batches is in-plane, but that this effect is more present for samples from batch 2. This could indicate that the adatom diffusion on the surface of batch 2 is faster than on the surface of batch 1 as the ion flux towards nuclei from the in-plane direction is larger than that of the out-of-plane direction. It is important to be aware of this initial growth behaviour when more complex 3D structures are envisioned.

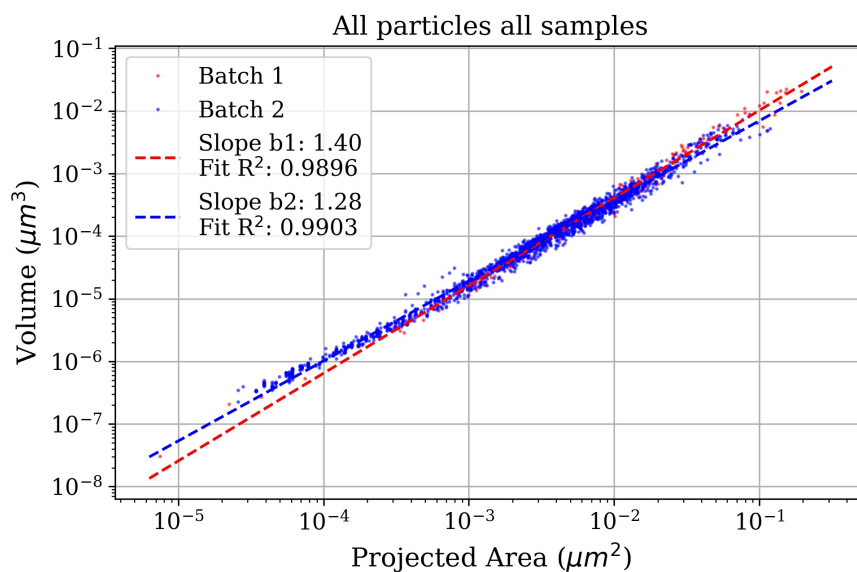


Figure 5.12: Particle volume versus its projected area from several AFM measurements on samples from both ITO batches. The slope of the fit is an indication for the growth direction.

In this work it was shown that the substrate, electrolyte, and electrochemical parameters all play a role in the electrodeposition of Ag on ITO when using the double-pulse technique. It is important to characterize the ITO substrate as it was found with XRD that the polycrystallinity can affect both the nucleation mechanism and the growth direction. In particular, this was observed for electrodeposition experiments with a saccharin-based electrolyte. To distinguish ITO batches with different preferred crystal orientations the peak height ratio between the (222) and (400) plane was calculated. Batch 1 shows a ratio for these peaks of 1, while batch 2 shows a ratio of 5.

By varying the overpotential of the first pulse (E_n) from 0.2 to -0.883 V vs. Ag/AgCl and keeping the other electrochemical parameters constant, Ag nanoparticles were obtained. The projected area and amount of these particles were analyzed with SEM and particle sizes in the range of $10^2 - 10^5 \text{ nm}^2$ were obtained with particle densities of $10^5 - 10^9 \text{ cm}^{-2}$. It was found that upon increasing E_n the particle size would decrease, while the particle density would increase. This could be explained by increased diffusion-limited growth in which the high reaction rate creates closely spaced nuclei that compete with each other for ions.

Samples from both batch 1 and batch 2 followed the same trend for E_n below -0.4 V. Above this potential, however, batch 2 started to show less decrease in particle density and less increase in particle size. This suggests that one of the batches exhibits a change of nucleation mechanism. To investigate this further, reported growth models were fitted to the chronoamperometry data. It was confirmed that upon increasing E_n a mechanistic transition from progressive to instantaneous nucleation occurred for batch 1, while the nucleation for batch 2 remained instantaneous over the whole potential range. Finally, the preferred growth direction was determined by analyzing the particles with AFM. It was found that both ITO batches facilitated in-plane growth, but that this effect was more pronounced for batch 2.

These results show that the overpotential of the first pulse can be used to control the particle density and particle size of Ag nanoparticles on ITO. However, to do this accurately, the surface properties of ITO should be identified as they have an effect on the nucleation and growth. Further research could extend the surface characterization of ITO beyond XRD, for instance, with Kelvin-probe force microscopy (KPFM). In addition, it would be interesting to modify the surface potential and Appendix A8 briefly discusses preliminary results with a self-assembled monolayer. On a long-term scale, it might be interesting to repeat this study with electrodepositions of other metals.

- [1] Future Market Insights, *2021 Analysis and Review: Electroplating Market by Substrate – Base Metal Plating and Plastic Plating for 2021 - 2031*, REP-GB-936, 2021, <https://www.futuremarketinsights.com/reports/electroplating-market>.
- [2] A. Leiden, S. Kölle, S. Thiede, K. Schmid, M. Metzner, and C. Herrmann, *Model-based analysis, control and dosing of electroplating electrolytes*, *International Journal of Advanced Manufacturing Technology* **111**, 1751 (2020).
- [3] StrategyR, *Electroplating - Global Market Trajectory and Analytics*, MCP-6112, 2021, <https://www.strategyr.com/market-report-electroplating-forecasts-global-industry-analysts-inc.asp>.
- [4] C. Raub, *The history of electroplating*, Butterworth-Heinemann Ltd, 1993.
- [5] E. Jaszczak, Ż. Polkowska, S. Narkowicz, and J. Namieśnik, *Cyanides in the environment—analysis—problems and challenges*, *Environmental Science and Pollution Research* **24**, 15929 (2017).
- [6] A. Mulone, J. Hildenbrand, and U. Klement, *Electrodeposition: three steps towards sustainability*, *Transactions of the Institute of Metal Finishing* **98**, 108 (2020).
- [7] R. Bomparola, S. Caporali, A. Lavacchi, and U. Bardi, *Silver electrodeposition from air and water-stable ionic liquid: An environmentally friendly alternative to cyanide baths*, *Surface and Coatings Technology* **201**, 9485 (2007).
- [8] F. Z. Ren, L. T. Yin, S. S. Wang, A. A. Volinsky, and B. H. Tian, *Cyanide-free silver electroplating process in thiosulfate bath and microstructure analysis of Ag coatings*, *Transactions of Nonferrous Metals Society of China (English Edition)* **23**, 3822 (2013).
- [9] N. Fishelson, A. Inberg, N. Croitoru, and Y. Shacham-Diamand, *Highly corrosion resistant bright silver metallization deposited from a neutral cyanide-free solution*, *Microelectronic Engineering* **92**, 126 (2012).
- [10] X. Li, Z. Zhang, S. Suo, Y. Qiao, B. Du, H. Deng, Z. Hao, and H. Luo, *Microstructure of silver coating of cyanide-free brush plating based on multicomponent coordination system*, *IOP Conference Series: Materials Science and Engineering* **688** (2019).

-
- [11] M. Ijaz, M. Zafar, and T. Iqbal, *Green synthesis of silver nanoparticles by using various extracts: a review*, *Inorganic and Nano-Metal Chemistry* **51**, 744 (2020).
- [12] J. C. Bian, Z. Li, Z. D. Chen, H. Y. He, X. W. Zhang, X. Li, and G. R. Han, *Electrodeposition of silver nanoparticle arrays on ITO coated glass and their application as reproducible surface-enhanced Raman scattering substrate*, *Applied Surface Science* **258**, 1831 (2011).
- [13] H. Lu, G. Han, J. Cao, M. Jin, Q. Ma, E. M. Akinoglu, X. Wang, L. Nian, G. Zhou, and L. Shui, *Large-Area and Patternable Nano-Dot Array from Electrolysis of ITO Film for Surface-Enhanced Raman Spectroscopy*, *Nanoscale Research Letters* **15** (2020).
- [14] G. Sandmann, H. Dietz, and W. Plieth, *Preparation of silver nanoparticles on ITO surfaces by a double-pulse method*, *Journal of Electroanalytical Chemistry* **491**, 78 (2000).
- [15] N. Y. Hau, Y. H. Chang, Y. T. Huang, T. C. Wei, and S. P. Feng, *Direct electroplated metallization on indium tin oxide plastic substrate*, *Langmuir* **30**, 132 (2014).
- [16] A. J. Bard and L. R. Faulkner, *Electrochemical Methods: Fundamentals and Applications*, Wiley Textbooks, second edition, 2000.
- [17] C. G. Zoski, *Handbook of Electrochemistry*, Elsevier, first edition, 2007.
- [18] J. M. Pingarrón, J. Labuda, J. Barek, C. M. Brett, M. F. Camões, M. Fojta, and D. B. Hibbert, *Terminology of electrochemical methods of analysis (IUPAC Recommendations 2019)*, *Pure and Applied Chemistry* **92**, 641 (2020).
- [19] R. G. Compton and C. E. Banks, *Understanding Voltammetry*, Manchester Metropolitan University, second edition, 2010.
- [20] E. Budevski, G. Staikov, and W. J. Lorenz, *Electrocrystallization Nucleation and growth phenomena*, *Electrochimica Acta* **45**, 2559 (2000).
- [21] A. Milchev, *Electrochemical phase formation: Classical and atomistic theoretical models*, *Nanoscale* **8**, 13867 (2016).
- [22] A. Milchev, *Nucleation phenomena in electrochemical systems: kinetic models*, *Chem-Texts* **2**, 1 (2016).
- [23] H. Y. Tsai, C. N. Hsu, C. R. Li, Y. H. Lin, W. T. Hsiao, K. C. Huang, and J. A. Yeh, *Article surface wettability and electrical resistance analysis of droplets on indium-tin-oxide glass fabricated using an ultraviolet laser system*, *Micromachines* **12**, 1 (2021).
- [24] A. Scheludko and T. M., *Bull. Acad. Bulg. Sci. Phys.* (1952).
- [25] R. M. Penner, *Brownian dynamics simulations of the growth of metal nanocrystal ensembles on electrode surfaces in solution: 2. The effect of deposition rate on particle size dispersion*, *Journal of Physical Chemistry B* **105**, 8672 (2001).
-

-
- [26] G. J. Hills, D. J. Schiffrin, and J. Thompson, *Electrochemical nucleation from molten salts-II: Time dependent phenomena in electrochemical nucleation*, [Electrochimica Acta](#) **19**, 671 (1974).
- [27] A. Milchev, B. Scharifker, and G. Hills, *A potentiostatic study of the electrochemical nucleation of silver on vitreous carbon*, [Journal of Electroanalytical Chemistry and Interfacial Electrochemistry](#) **132**, 277 (1982).
- [28] H. Liu and R. M. Penner, *Size-selective electrodeposition of mesoscale metal particles in the uncoupled limit*, [Journal of Physical Chemistry B](#) **104**, 9131 (2000).
- [29] H. Liu, F. Favier, K. Ng, M. P. Zach, and R. M. Penner, *Size-selective electrodeposition of meso-scale metal particles: A general method*, [Electrochimica Acta](#) **47**, 671 (2001).
- [30] M. Ueda, H. Dietz, A. Anders, H. Knepe, A. Meixner, and W. Plieth, *Double-pulse technique as an electrochemical tool for controlling the preparation of metallic nanoparticles*, [Electrochimica Acta](#) **48**, 377 (2002).
- [31] S. C. Kung, W. Xing, K. C. Donovan, F. Yang, and R. M. Penner, *Photolithographically patterned silver nanowire electrodeposition*, [Electrochimica Acta](#) **55**, 8074 (2010).
- [32] J. L. Fransaer and R. M. Penner, *Brownian dynamics simulation of the growth of metal nanocrystal ensembles on electrode surfaces from solution. I. Instantaneous nucleation and diffusion-controlled growth*, [Journal of Physical Chemistry B](#) **103**, 7643 (1999).
- [33] M. Aliofkhazraei and A. S. H. Makhlof, [Handbook of Nanoelectrochemistry](#), Springer International Publishing, Cham, 2016.
- [34] F. G. Cottrell, *Der Reststrom bei galvanischer Polarisierung, betrachtet als ein Diffusionsproblem*, [Zeitschrift für Physikalische Chemie](#) **42U**, 385 (1903).
- [35] B. Scharifker, *Theoretical and experimental studies of multiple nucleation*, [Electrochimica Acta](#) **28**, 879 (1982).
- [36] J. Ustarroz, X. Ke, A. Hubin, S. Bals, and H. Terryn, *New insights into the early stages of nanoparticle electrodeposition*, [Journal of Physical Chemistry C](#) **116**, 2322 (2012).
- [37] M. Avrami, *Kinetics of Phase Change. I General Theory*, [The Journal of Chemical Physics](#) **7**, 1103 (1939).
- [38] M. Avrami, *Kinetics of Phase Change. II Transformation-Time Relations for Random Distribution of Nuclei*, [The Journal of Chemical Physics](#) **8**, 212 (1940).
- [39] *Electrochemical nucleation with diffusion-limited growth. Properties and analysis of transients*, [Electrochemistry Communications](#) **2**, 85 (2000).
- [40] B. Scharifker and J. Mostany, *Three-dimensional nucleation with diffusion controlled growth Part I. Number density of active sites and nucleation rates per site*, [Journal of electroanalytical chemistry](#) **177**, 13 (1984).
-

-
- [41] L. Heerman and A. Tarallo, *Theory of the chronoamperometric transient for electrochemical nucleation with diffusion-controlled growth*, [Journal of Electroanalytical Chemistry](#) **470**, 70 (1999).
- [42] M.V.Mirkin and P.A.Nilov, *Three-dimensional nucleation and growth under controlled potential*, [Journal of Electroanalytical Chemistry](#) **283**, 35 (1990).
- [43] P. J. Flory, *Predissociation of the oxygen molecule*, [The Journal of Chemical Physics](#) **4**, 23 (1936).
- [44] R. Chen, C. Yang, W. Cai, H.-Y. Wang, J. Miao, L. Zhang, S. Chen, and B. Liu, *Use of Platinum as the Counter Electrode to Study the Activity of Nonprecious Metal Catalysts for the Hydrogen Evolution Reaction*, [ACS Energy Letters](#) **2**, 1070 (2017).
- [45] J. I. Goldstein, D. E. Newbury, P. Echlin, D. C. Joy, C. E. Lyman, E. Lifshin, L. Sawyer, and J. R. Michael, [Scanning Electron Microscopy and X-ray Microanalysis](#), Springer US, Boston, MA, 2003.
- [46] M. Ezzahmouly, A. Elmoutaouakkil, M. Ed-Dhahraouy, H. Khallok, A. Elouahli, A. Mazurier, A. ElAlbani, and Z. Hatim, *Micro-computed tomographic and SEM study of porous bioceramics using an adaptive method based on the mathematical morphological operations*, [Heliyon](#) **5**, e02557 (2019).
- [47] Bruker, *Application Note # 133 Introduction to Bruker's ScanAsyst and PeakForce Tapping AFM Technology*, Bruker Application Note , 1 (2011).
- [48] P. M. Parikh and S. P. Mukherji, *The determination of saccharin*, [The Analyst](#) **85**, 25 (1960).
- [49] R. S. Nicholson, *Theory and Application of Cyclic Voltammetry for Measurement of Electrode Reaction Kinetics.*, [Analytical Chemistry](#) **37**, 1351 (1965).
- [50] R. J. Klingler and J. K. Kochi, *Electron-transfer kinetics from cyclic voltammetry. Quantitative description of electrochemical reversibility*, [The Journal of Physical Chemistry](#) **85**, 1731 (1981).
- [51] I. Lavagnini, R. Antiochia, and F. Magno, *An Extended Method for the Practical Evaluation of the Standard Rate Constant from Cyclic Voltammetric Data*, [Electroanalysis](#) **16**, 505 (2004).
- [52] Z. Zhang and M. G. Lagally, *Atomistic processes in the early stages of thin-film growth*, [Science](#) **276**, 377 (1997).

ACKNOWLEDGEMENTS

First of all, thank you Esther for letting me join your unique research group in these weird times. It definitely takes some mutual trust to conduct a project during a pandemic. Remarkably, it was one of the projects in which I felt really connected to a research group and this is definitely not only due to the great atmosphere at AMOLF. For that, I dearly have to thank everyone else from the 3DPhotovoltaics group as well, Daphne (enthusiastic, but always realistic), Jos (the inspiring inspector), Mark (helpful and pleasant to share an office with), Jelena (supportive and always up for a chat), Alex (with his inexhaustible source of ideas), Juliane (who seems to be an excellent collaborator), Marco (always up for discussion), Blaise (who showed what perseverance on the lab entails), Nasim (always smiles) and Daniël (who is eager to learn about your project, even though he has nothing to do with it).

Especially, I want to thank Yorick for his excellent supervision and answers on my endless stream of questions. I could not have wished for a better help during the exploration of a scientific field that was rather new to me. Thanks a lot!

Other people at AMOLF that I want to thank here are Balázs for helping me with IR and Jan for performing SFG measurements. From ARCNL I would like to thank Stefan for performing XPS measurements for me, and Roland for giving me this opportunity.

So far, I have had an amazing time at AMOLF and I hope that this can continue during my PhD.

A1 Reference electrode performance

The equilibrium potential of the leakless ET072-1 micro Ag/AgCl electrode shifted over time and Figure A1 shows the open circuit potential (OCP) against the radiometer analytical XR300 Ag/AgCl reference electrode. When the OCP starts to saturate it is necessary to replace the micro electrode.

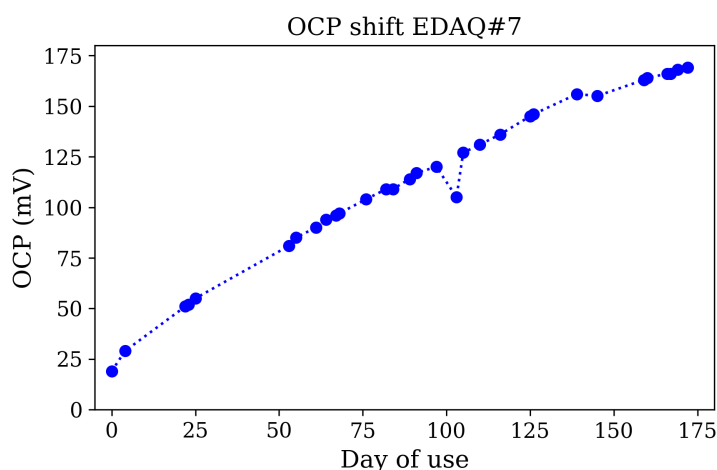


Figure A1: Open circuit potential (OCP) of the leakless ET072-1 micro Ag/AgCl electrode against the radiometer analytical XR300 Ag/AgCl reference electrode versus time.

A2 Miscellaneous

First, a plot of the particle density (Figure A2) is shown that compares the effect of using 2 week old electrolyte, contacting only one of the four points to the sample and coating the sample with a monolayer (more on this in section A8). It becomes clear that the electrolyte age does not affect the particle density, while the other two variations show an unwanted decrease in particle density.

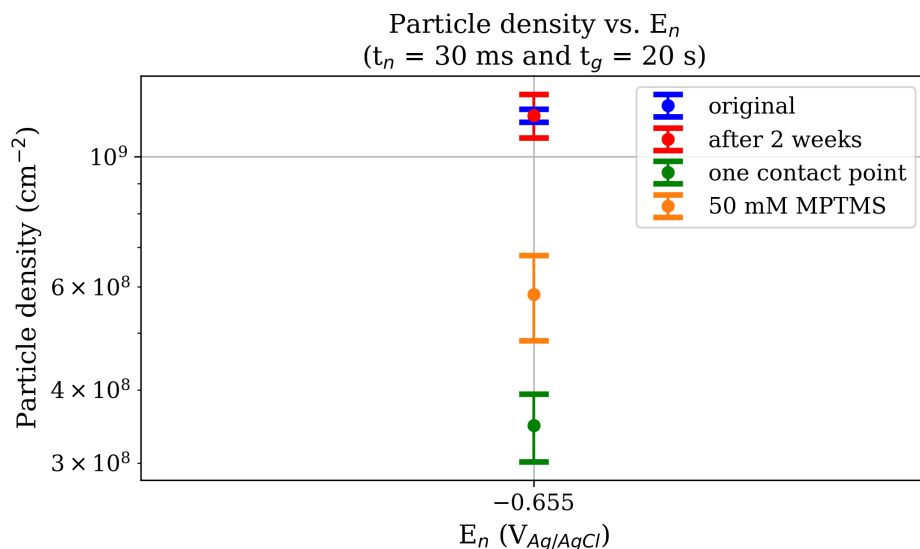


Figure A2: The particle density for using 2 week old electrolyte, contacting only one of the four points to the sample and coating the sample with a monolayer.

Table A1: Parameter overview saccharin-based electrolyte. Arrows indicate an increase (up) or decrease (down) for each parameter.

	ρ	θ	Size	Mean radius	σ_{abs}
$\uparrow E_n$	\uparrow	\uparrow	\downarrow	\downarrow	\downarrow
$\uparrow t_n$	-	\uparrow	-	-	-
\uparrow pH	-	-	-	-	-
\uparrow [Ag]	-	\uparrow	\uparrow	\uparrow	\uparrow

Then, the corresponding particle densities for Figure 5.3 are shown in Figure A3, which confirms that t_n does not affect the particle density in this range, while E_n does.

Finally, other electrochemical parameters that were swept are discussed here briefly. Table A1 shows a schematic overview for all parameters that were swept with the saccharin-based electrolyte.* It can be observed that an increase in t_n only slightly increased the surface coverage, while the pH did not affect any of these parameters at all. More interestingly, the Ag concentration does not affect the particle density, while it hugely increases the surface coverage and barely increases the particle size. Therefore, varying this parameter is most interesting for growing larger structures of Ag on ITO.

Table A2 includes the parameters that were swept with the Clean Earth electrolyte.

*The amount of nucleation pulses was varied as well, but the potentiostat was not able to apply these without a stabilization time. Therefore, distorted potential pulses were obtained and the measurements were disregarded.

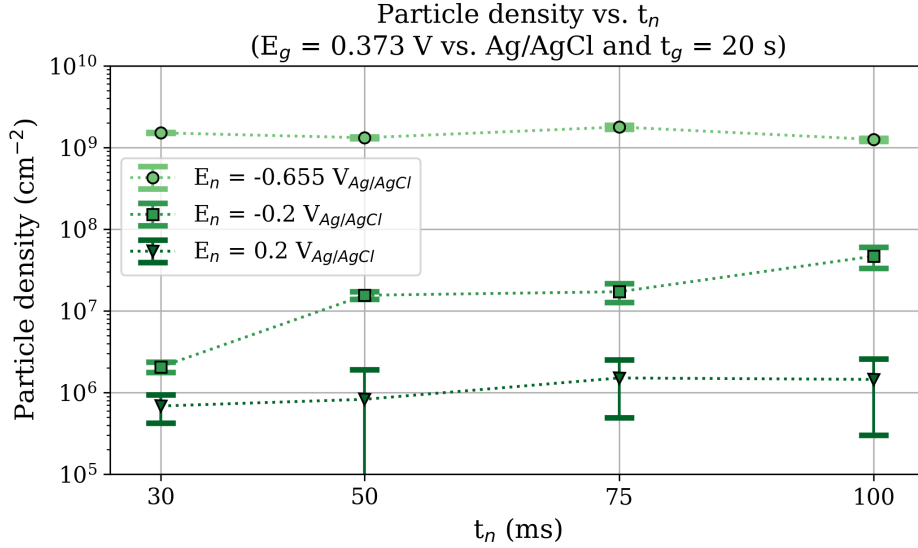


Figure A3: Particle densities corresponding to Figure 5.3.

Table A2: Parameter overview Clean Earth electrolyte. Arrows indicate an increase (up) or decrease (down) for each parameter.

	ρ	θ	Size	Mean radius	σ_{abs}
$\uparrow t_g$	$\uparrow\downarrow$	\uparrow	\uparrow	\uparrow	\uparrow
$\uparrow t_n$	\uparrow	\uparrow	\downarrow	\downarrow	\uparrow
\uparrow [MPTMS]	\uparrow	-	\downarrow	\downarrow	\downarrow

A large arrow for t_n for the particle density is shown, as it was found that the particle density without nucleation pulse was 10^5 , while with nucleation pulse it was 10^{10} . Coating the samples with a monolayer (section A8) slightly increases the particle density, while the coverage is not affected and the other parameters slightly decrease (similar to E_n for the saccharin-based electrolyte). Increasing t_g first leads to an increase in particle density, but after 5 s it decreases again. This can be explained by progressive nucleation in the first 5 s and diffusional coupling/merging after this point. Since, here the time-dependent component is present it is also possible to plot the relative standard deviation of the mean radius versus the mean radius. According to Ueda et al. it is possible to determine the extend of diffusional coupling from the slope of this plot. The trend in Figure A4 increases, which indicates that increased diffusional coupling could play a role in this system. However, this could not be confirmed with modeling the chronoamperometry data as the current response was too complex, likely due to all the organic additives that influence the current.

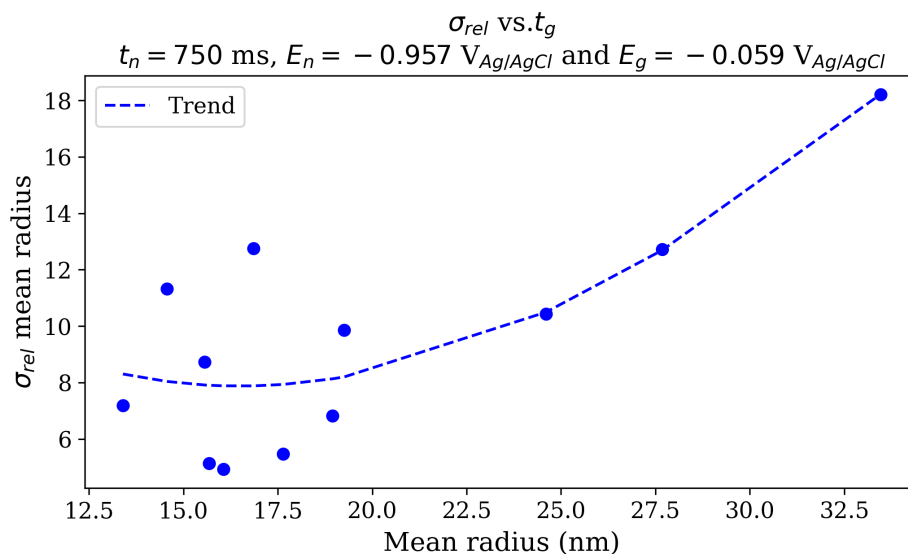


Figure A4: Relative standard deviation (σ_{rel}) mean radius vs. mean radius for varying t_g for the Clean Earth electrolyte.

A3 Potentiostat performance

Three potentiostats were available, two from Biologic but different series (SP-200 and SP-300) and one from CH Instruments. According to their specifications, all of them should be able to perform the experiments reported in this thesis. However, different results from electrodeposition experiments were obtained when using the CH potentiostat opposed to either the SP-200 or SP-300. The difference was more prominent for depositions that contained a short nucleation pulse. Therefore, all potentiostats were tested on their performance individually by monitoring the potential with one of the other potentiostats. In the case of using a potentiostat as voltmeter no significant difference in performance was observed. Moreover, the SP-200 and SP-300 showed no difference in chronoamperometry experiments. As the latter was used in this work it is compared to the CH potentiostat in Figure A5. It is clear that the CH potentiostat is not suited for short nucleation pulses as it gives pulse durations that are slightly higher up to 1 s. The SP-300 on the other hand follows the expected pulse duration up to a minimum of 29 ms. Therefore, it was decided to use pulses of minimal 30 ms throughout this project.

Still, the potential scheme of such short pulses is unclear according to the SP-300 itself (Figure A6), while monitoring with the CH indicates that the applied potential matches the wanted potential scheme perfectly. Most of the chronoamperometry experiments with the SP-300 in this thesis were monitored with the CH to make sure that the correct potential was applied for the right duration.

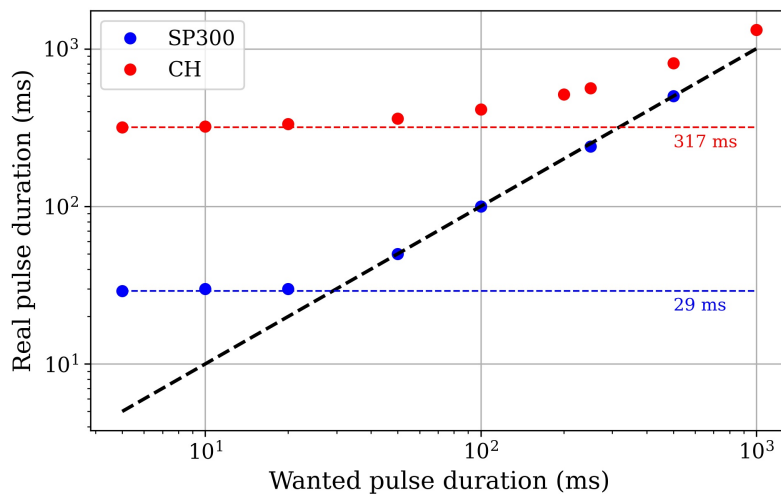


Figure A5: Wanted and obtained nucleation pulse duration for both the CH and SP-300 potentiostat. The dashed black line shows the expected pulse duration.

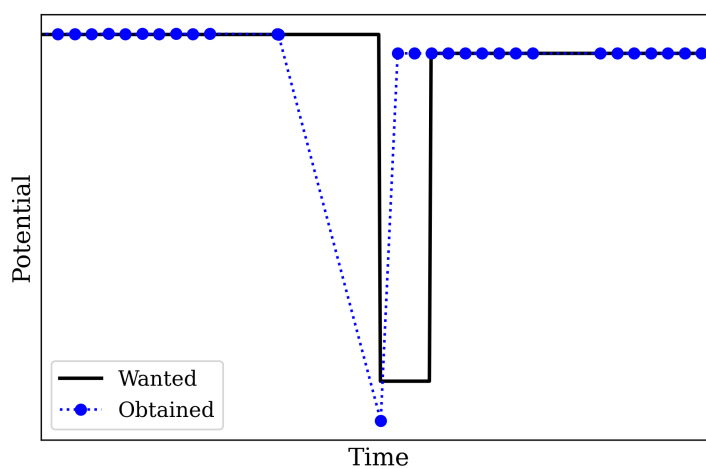


Figure A6: Wanted, monitored and obtained potential scheme, zoomed in on the 30 ms pulse.

A4 EC-lab

Figure A7 shows typical settings that were used for experiments. In the safety/advanced settings the user can set overload barriers and averaging over measurement points.

a)

b)

Figure A7: Settings in EC-lab for (a) a nucleation pulse for chronoamperometry and (b) one scan rate for cyclic voltammetry.

A5 XRD peak height ratios

Figure A8 shows the calculated XRD peak height ratios for all samples used in the nucleation study in the main text.

A6 Cyclic voltammetry models

As Butler-Volmer kinetics show an exponential behaviour (Equation 2.12) both the reduction and oxidation part can be fitted with an equation of the form $y = ax^{b+c}$. However, the reduction part of experimental data in this research is more valid as Butler-Volmer kinetics are based on ion-to-ion reactions and these kinetics resemble ion-to-solid kinetics more than solid-to-ion kinetics. It was found that in the obtained CV for the Clean Earth electrolyte data $f_{red} + f_{ox} = \frac{nF}{RT}$ did not hold so that a correction factor was needed, which remained more or less constant within cycles, but changed significantly among experiments. By fitting the data for a range of concentrations (as this was unknown) the rate constant of the reaction

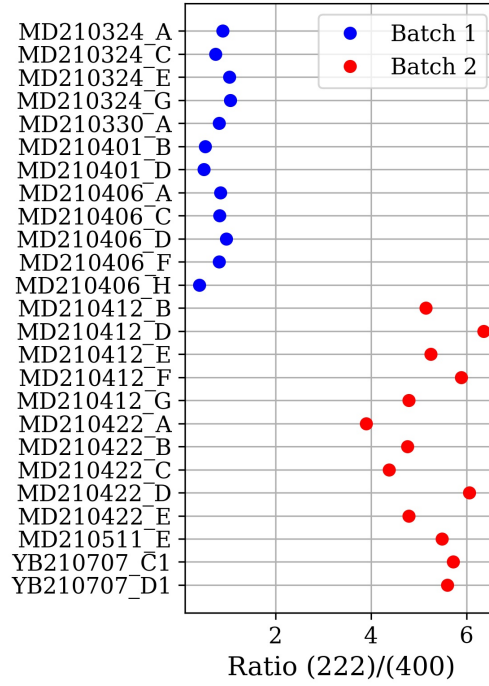


Figure A8: The XRD peak height ratios for all samples that were used for the nucleation study.

was computed.[†]

According to the shape and difference between the reduction and oxidation peak currents the system is quasi-reversible, which means that the following form of the Randles-Ševčík equation can be used to calculate the diffusion coefficient if the concentration is known:

$$J_p = 0.4985nFC\sqrt{\alpha v D_0 \frac{nF}{RT}} \quad (\text{A1})$$

Again, values can be computed for a concentration range. However, it is possible to calculate D_0 for each cycle separately or to perform a linear fit of each experiment in which J_p is plotted against $\sqrt{\alpha v}$. For the latter, the average of the asymmetry factor α from the cycles in that particular experiment is used. This can be done again for both the reduction and oxidation part, resulting in D_0 calculated from single cycles, the average of these values, and D_0 calculated with slopes from fits.

Subsequently, it is possible to calculate the rate constant with the Nicholson method [49]:

$$\Psi = \frac{k^0}{\sqrt{\pi D v \frac{nF}{RT}}} \quad (\text{A2})$$

[†]It was not possible to do this analysis with the saccharin-based electrolyte as multiple events occurred in the CV.

This Ψ is one of the variables that determines the shape of a CV curve and Lavagnini et al. developed an empirical correlation between Ψ and ΔE_p [51]:

$$\Psi = \frac{-0.6288 + 0.0021n\Delta E_p}{1 - 0.0017n\Delta E_p} \quad (\text{A3})$$

This equation holds only for quasi-reversible systems and curves with $\Psi < 7$ are too reversible, while curves with $\Delta E_p > 212\text{mV}$ are too irreversible. For the latter case, Klingler and Kochi developed an extension of Ψ [50]:

$$\Psi = 2.18\sqrt{\alpha/\pi}e^{(-\alpha^2\Delta E_p\frac{nF}{RT})} \quad (\text{A4})$$

Data from each cycle is checked for its compatibility with calculating Ψ and by performing a linear fit of Ψ plotted against $\frac{1}{\sqrt{v}}$, k^0 is calculated for both the average D_0 and the fitted D_0 for both reduction and oxidation parts. The script to both these analyses is available on request.

A7 ImageJ analysis

After performing chronoamperometry the samples were characterized with SEM and a typical SEM image is shown in Figure A9. This appendix briefly elaborates on the analysis of such images with ImageJ. First, the scale is set which can be easily done by drawing a line along the scale bar. The exact start and end can be found by zooming in (*ctrl+mouse scrol*) and after selecting *Analyze>Set scale* the *distance in pixels* should be an integer. If not, this can be corrected manually and after filling in the *known distance* and *unit of length* the scale selection is done. Then, the image is cropped to remove the information bar by selecting only the actual image with a *rectangular selection* and duplicating this with *ctrl+shift+D*. It is converted to an 8-bit image via *Image>Type>8-bit* and with *ctrl+shift+T* the threshold menu is opened. Here, the particles can be selected by adjusting the *sliders* and in this work all images had a *dark background*. After clicking *Apply* a black and white image is obtained (Figure A10). It might be that some particles have holes or that also organic (dust) particles are black. In the former case one can use *Process>Binary>Fill holes* and in the latter case the *drawing tools* can be used to remove unwanted particles. Besides that, particles might overlap, which can be solved manually with the *drawing tools* but if the overlap is not too much *Process>Binary>Watershed* might be sufficient. Subsequently, with *Analyze>Set measurements* one can choose which parameters should be extracted with *Analyze>Analyze particles*. In this menu it is possible to set a threshold for what particle sizes should be taken into account. Here, it was chosen to analyze particles with at least 6 pixel units. Finally, the image area can be measured with *ctrl+M* and these *Results* are saved as a comma-separated .csv file.

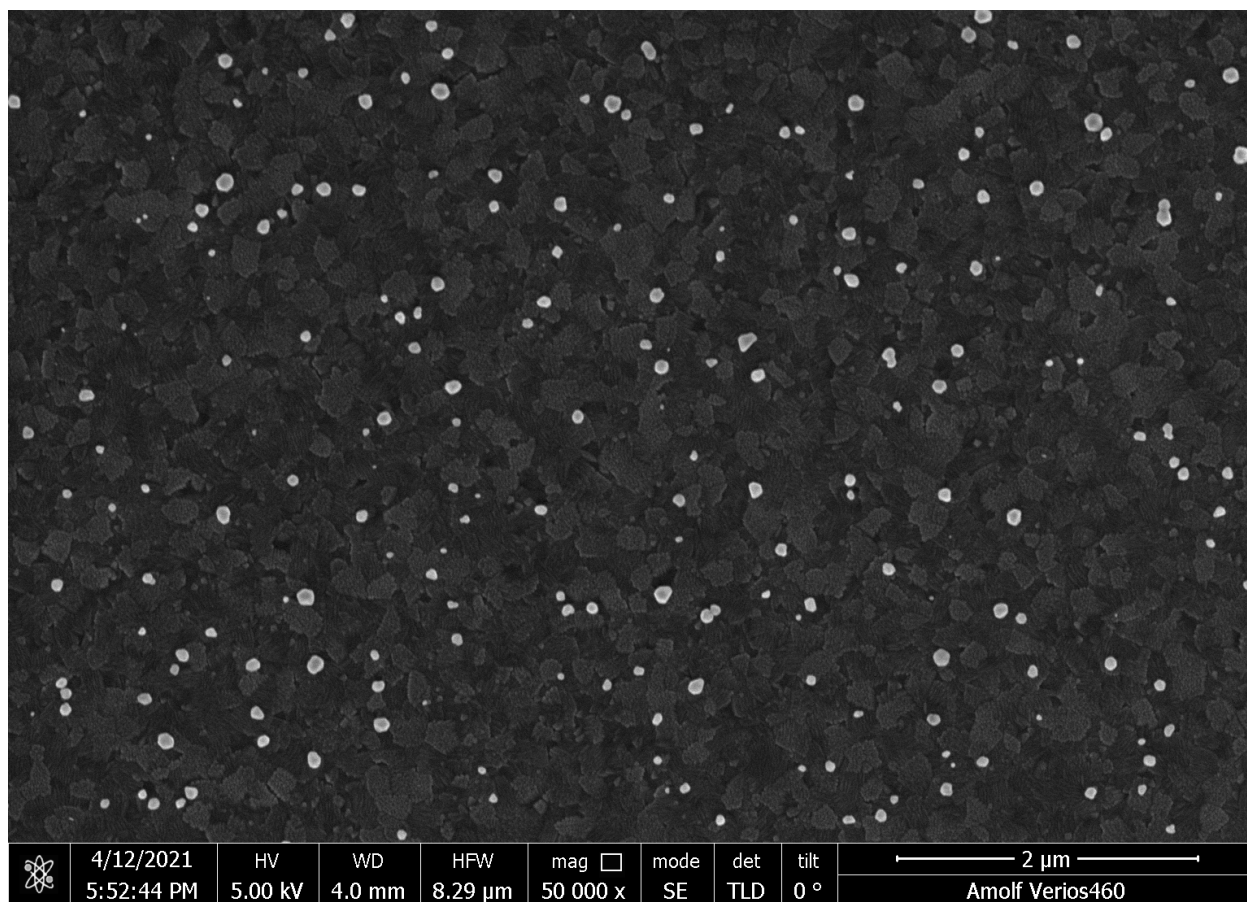


Figure A9: Unprocessed SEM image of Ag nanoparticles on ITO.

A8 Self-assembled monolayers

An attempt was made to synthesize self-assembled monolayers with 3-mercaptopropyl trimethoxysilane (MPTMS) according to the method of Hau et al. [15]. The ITO samples were immersed in ethanol solutions for 30 min with different concentrations of MPTMS (ranging from 25 to 100 mM). Hau et al. analyzed the result with contact angle measurements and electrochemical impedance spectroscopy. However, they did not report any elemental analysis and it was found that the contact angle of water on the ITO samples in this work was already heavily affected by ozone cleaning, which resulted in heavily increased wettability.

It is beyond the scope of this Appendix to go into detail on all the characterization techniques that have been employed (AFM, ATR-IR, PM-IRRAS, SFG, XPS, KPFM, CAM). Nevertheless, it can be concluded that characterization of a SAM on ITO is quite challenging.

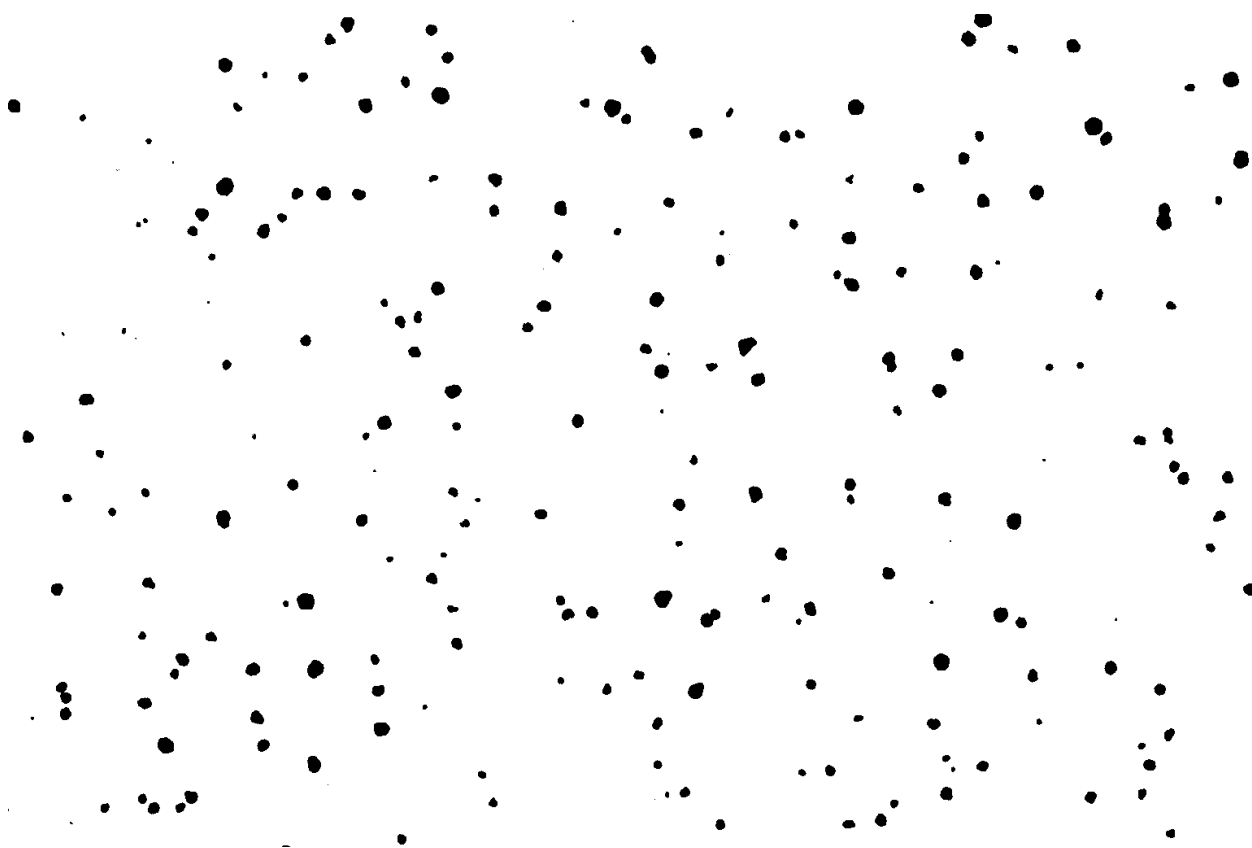


Figure A10: *Processed SEM image of Ag nanoparticles on ITO.*